The Greater Himalayan thrust belt: Insight into the assembly of the exhumed Himalayan metamorphic core, Modi Khola valley, central Nepal.

Sudip Shrestha[1*], Kyle P. Larson[1], Aaron J. Martin[2], Carl Guilmette[3], Matthijs A. Smit[4], John M. Cottle[5]

[1]Earth and Environmental Sciences, University of British Columbia Okanagan, 3247 University Way, Kelowna, British Columbia, V1V 1V7, Canada
[2]División de Geociencias Aplicadas, IPICYT, CP 78216 San Luis Potosí, Mexico
[3]Géologie et génie géologique, Université Laval, 1065 avenue de la Médecine, Québec, G1V 0A6, Canada
[4]Department of Earth, Ocean and Atmospheric Science, University of British Columbia Vancouver, 2020-2207 Main Mall, Vancouver, British Columbia, V6T 1Z4, Canada
[5]Department of Earth Science, University of California, Santa Barbara, CA 93106–9630, USA

Corresponding author: Sudip Shrestha (sudip.shrestha@alumni.ubc.ca)

Key Points:

- Structural breaks within exhumed metamorphic core in the Modi Khola valley include Sinuwa thrust, Bhanuwa fault and Main Central thrust
- Rocks record similar prograde but varying history of anatexis, cooling and exhumation indicating down-structural migration of metamorphism
- P-T-t paths outline in-sequence thrusting, development of the Greater Himalayan thrust belt followed by reactivation of the Bhanuwa fault

[*] Current address - Fipke Laboratory for Trace Element Research, University of British Columbia Okanagan, 3247 University Way, British Columbia, V1V 1V7, Canada

Abstract

Strike-parallel discontinuities within the Himalayan metamorphic core are interpreted to reflect thrust-sense movement. There is, however, disagreement on the nature and sense of movement across one such structure in central Nepal, which has hampered efforts to understand its kinematics and potentially correlate it with structures at similar structural levels. Using an integrated approach, this study characterizes multiple structural breaks in the Modi Khola region. Thermobarometric calculations combined with petrochronological investigation show that the rocks across the Sinuwa thrust record similar histories with prograde garnet growth ca. 35 Ma and peak pressures of ~ 11.0 kbar, anatexis at ca. 28 Ma followed by cooling and exhumation between ca. 24 and 15 Ma. Whereas, rocks below the Bhanuwa fault record similar garnet growth at ca. 35 Ma and pressures of ~11.5 kbar, but experienced melting and retrogression after ca. 21 Ma. Finally, the rocks in the footwall of Main Central thrust record prograde metamorphism ca. 17 - 13 Ma with peak pressures of ~ 7.0 kbar. This down-structural migration of prograde metamorphism, anatexis, and subsequent cooling and exhumation of the footwall is consistent with models of progressive underplating and in-sequence thrusting. Paired with published cooling ages across the Bhanuwa fault, results from this study indicate reactivation of normal-sense motion across the structure later during mid-late Miocene time. This new dataset shows that the final assembly of the Himalayan metamorphic core is a result of progressive deformation and juxtaposition of multiple thrust sheets. We refer to this as the Greater Himalayan thrust belt.

1. Introduction

The exhumed Himalayan metamorphic core (HMC) is a package of pervasively deformed and metamorphosed rocks that record the Cenozoic tectonometamorphic evolution along the Himalaya (Cottle et al. 2009; From et al., 2014). The recognition of multiple strike-parallel discontinuities within the HMC led to a significant improvement in the knowledge of how the Himalayan mid-crust accommodated convergence (Larson et al., 2015; Montomoli et al., 2015); they demonstrate that the evolution of the HMC is significantly more complex than previously thought (e.g. Hodges, 2000; Searle et al., 2008; Yin and Harrison, 2000) and was to a large extent controlled by discrete high strain zones that can now be traced along the length of the Himalayan mountain belt (e.g. Larson et al., 2015; Montomoli et al., 2015).

Two general types of discontinuities have been identified across the orogen (Cottle et al., 2015; Larson et al., 2015; Montomoli et al., 2015): one comprises late Oligocene - early Miocene in-sequence thrusts formed during the propagation of thrusts towards the foreland (e.g. Carosi et al., 2010; Iaccarino et al., 2017; Imayama et al., 2012; Larson & Cottle, 2014; Martin et al., 2010; Montomoli et al., 2013; Rubatto et al., 2013; Shrestha et al., 2017; Yakymchuk & Godin, 2012) and the other consists of discontinuities that are typically younger, mid-to-late Miocene out-of-sequence structures (e.g. Ambrose et al., 2015; Grujic et al., 2002; 2011; Larson, 2018; Larson et al., 2016; Long & McQuarrie, 2010; Mukherjee et al., 2012; Rubatto et al., 2013; Wang et al., 2013). While the former type of discontinuity typically occurs in the mid-to-lower HMC, the out-of-sequence structures exclusively occur in the upper portion (e.g. Carosi et al., 2010; Hodges et al., 1996; Larson, 2018; Larson et al., 2015; Montomoli et al., 2015; Mukherjee et al., 2012).

Both types of discontinuities within the HMC are generally interpreted to reflect thrust-sense motion (see Larson et al., 2015; Montomoli et al., 2015), however, there is disagreement on the sense of movement across at least one of these structures (Corrie & Kohn, 2011; Martin et al., 2010, 2015). In the Modi Khola region of Central Nepal, previous studies have identified two strike-parallel discontinuities within the HMC but have reached conflicting conclusions about one of the structures identified in this region (Fig. 1). Whereas the ‘Sinuwa thrust’ is reported to reflect thrust sense displacement

(Corrie & Kohn, 2011), the 'Bhanuwa fault' has been interpreted as a cryptic discontinuity with either top-to-the-north (Martin et al., 2010, 2015), or top-to-the-south (Corrie & Kohn, 2011) displacement across it. The lack of agreement on the sense of motion on the Bhanuwa fault has hampered efforts to correlate it with structures at similar structural levels observed elsewhere along the Himalaya (e.g. He et al., 2015). This has made it difficult to assess the lateral continuity of other recently identified tectonometamorphic discontinuities. Constraining the extent, continuity and shear sense of these structures is a fundamental step towards developing a more complete model for the evolution of the mountain belt and the processes by which such major orogenic system accommodate convergence.

This study takes an integrated approach towards characterizing the reported discontinuities in the Modi Khola region. We use the structural, metamorphic and geochronological record obtained through this work to quantify the sense of motion across the structures and discuss the implications of these findings for the evolution of the Himalayan mid-crust exposed in this part of the Himalaya.

2. Geological Setting

2.1. Lithotectonic units

The Modi Khola valley cuts the southern flank of the Annapurna range in Central Nepal (Fig. 1). The valley has long been the target of Himalayan researchers because it provides and easily accessible and well-exposed section through the HMC. From south to north, and structurally upward, this transect consists rocks of the Lesser Himalayan Sequence, the Greater Himalayan Sequence and the Tethyan Sedimentary Sequence (Yin and Harrison, 2000; see also Kohn, 2014a; Martin , 2017 for reviews of the lithotectonic classification of the Himalaya), all within a span of < 20 km (Corrie & Kohn, 2011; Hodges et al., 1996; Martin et al., 2005, 2010, 2015). The transect exposes greenschist facies rocks of the Lesser Himalayan Sequence and amphibolite facies rocks of the Greater Himalayan Sequence (Hodges et al., 1996; Martin et al., 2010) that records Cenozoic metamorphism and deformational histories. For the purposes of this study, and specifically because we are re-evaluating previous work and wish to avoid any potential confusion, we follow the mapping and lithostratigraphic descriptions of Hodges et al. (1996) as modified by Martin et al. (2010, 2011, 2015) and Corrie and Kohn (2011).

In the Modi Khola region, the low-grade metasedimentary rocks of the Lesser Himalayan Sequence have been classified into the lower Lesser Himalayan Sequence and upper Lesser Himalayan Sequence (Corrie & Kohn, 2011; Martin et al, 2010) (Fig. 1). The lower Lesser Himalayan Sequence consists of greenschist- to amphibolite- facies schist and quartzite with local orthogneiss of the Nawakot Unit overlain by metacarbonate and phyllite. The upper Lesser Himalayan Sequence consists of slate, phyllite and quartzite of the Tansen Unit (Corrie & Kohn, 2011; Martin et al., 2010).

The high-grade metamorphic rocks of the Greater Himalayan Sequence in the Modi Khola region are divided into three structural units (Corrie & Kohn, 2011; Hodges et al., 1996; Martin et al., 2010) (Fig. 1). The lowest, Unit I, consists of amphibolite-facies mica schist and migmatitic gneiss of pelitic and psammitic composition. This unit can be further separated into Units 1a - muscovite-rich with garnet that preserve growth zoning; 1b - migmatitic with garnet that displays flat major element profiles; and 1c - migmatitic with segregated leucosomes and garnet with compositionally homogeneous cores and retrograde rims (Corrie & Kohn, 2011). Unit II is a calcareous unit and consists of alternating layers of quartzite, marble and calc-silicates. Unit III comprises a thin band of pelitic schist and augen orthogneiss, which itself is interpreted to have intruded Unit II (Hodges et al, 1996; Martin et al., 2010). The felsic orthogneiss from Unit III in this region has been reported to record a Paleozoic magmatic crystallization age of ca. 500 Ma (Hodges et al., 1996).

The Modi Khola region also hosts several mapped normal- and thrust-sense structures (Fig. 1; Hodges et al., 1996; Corrie & Kohn, 2011; Martin et al., 2005, 2011, 2015). Of these, the major first order structures includes the Main Central thrust (MCT) and the South Tibetan Detachment System, which bound the lower and upper limits of the Greater Himalayan Sequence (Godin, 2003; Kohn, 2014a; Le Fort, 1975; Martin, 2017; Searle et al., 2008), separating it from the Lesser Himalayan Sequence to the south and the Tethyan Sedimentary Sequence to the north, respectively. In addition to the MCT, further intra-HMC structures are also identified in this area (see Corrie & Kohn, 2011 and Martin et al., 2010 for details. Two structures have been reported from the upper-HMC within the Greater Himalayan Sequence in Modi Khola region: the structurally lower Bhanuwa fault (Martin et al., 2010, 2015; Bhanuwa thrust: Corrie & Kohn, 2011) and the structurally higher Sinuwa thrust (Corrie & Kohn, 2011) (Fig. 1).

The identification of these additional intra-HMC structures and their associated kinematics was based primarily on P-T estimates. The P-T conditions were calculated using Garnet-Biotite-Muscovite-Plagioclase (GBMP), Garnet-Aluminosilicate-Quartz-Plagioclase (GASP) and/or Garnet-Biotite-Quartz-Plagioclase (GBSP) barometry and primarily Garnet-Biotite thermometry (Corrie & Kohn, 2011; Martin et al. 2010). Martin et al. (2010) reported an average P-T conditions of 15 kbar at ~ 720 ºC in the footwall of the Bhanuwa fault, with one specimen yielding pressures as high as 16 kbar and a temperature of ~ 820 ºC. In contrast, rocks in the hanging wall yielded P-T estimates of 11 kbar at 720 ºC that increased in temperature up structural section to 780 ºC. Based on these lower retrieved pressures from hanging wall rocks as well as slower hanging wall cooling inferred from longer retrograde diffusion profiles in garnet, Martin et al. (2010) proposed that the Bhanuwa fault accommodated normal-sense displacement. Later work on muscovite ^{40}Ar/^{39}Ar cooling ages across the structure indicated earlier cooling (~ 16 Ma) in the hanging wall and later cooling (~ 10 Ma) in the footwall, consistent with normal-sense movement (Martin et al., 2015). A different assessment was made by Corrie and Kohn (2011), who obtained an average P-T condition of 12 kbar and 650 ºC for the rocks below the Bhanuwa fault and 12.5 kbar and 735 ºC for rocks above with no significant change in P-T across the Sinuwa thrust. Monazite dates reported in the same study were interpreted to record prograde metamorphism in the footwall of the Bhanuwa fault between 21 and 16 Ma and between 29 and 24 Ma in the hanging wall; 22 - 17 Ma dates also from the hanging wall were interpreted to reflect post-anatexis cooling. Corrie and Kohn (2011) interpreted this combined dataset to record thrust sense motion on the Bhanuwa fault. The differences in the published interpretations has been ascribed to early thrust sense motion across the Bhanuwa fault ca. 23 - 19 Ma followed by normal sense motion thereafter (Martin et al., 2015). This interpretation, however, does not explain the discrepancy in the thermobarometric results from the different studies, calling into question its potential use in recognizing cryptic structures. Moreover, uncertainty around the kinematic history of the discontinuity is problematic for correlations with similar tectonometamorphic discontinuities across the Himalaya (Larson et al., 2015; Montomoli et al., 2015, and references therein).

This study re-examines the same rock specimens used by Martin et al. (2010; 2015) utilizing phase equilibria modelling, quartz inclusion in garnet (QuiG) barometry, monazite U-Th/Pb petrochronology, garnet Lu-Hf geochronology and trace element analysis. Ten specimens from a suite of rocks collected in the Modi Khola valley (Martin et al., 2010) were selected and examined during this work (Fig. 1). Four specimens (502035, 502074, 502073, 502072) were selected from the Lesser Himalayan Sequence rocks and six specimens (502071, 502069, 502068, 502067, 502050, 502056) from the Greater Himalayan Sequence rocks. All specimens, except the structurally highest 502056, are metapelite, and were collected from Unit I in the Greater Himalayan Sequence. Specimen 502056 is an orthogneiss collected from Unit III. Based on the mineral assemblage and suitability for a specific method, each specimen was analyzed using multiple different analytical procedures. Specimen 502072 was collected from a large block that may not have been outcrop. While we believe the block to be local (perhaps just slumped), we do not rely on data from this specimen for our overall interpretations. We do, however, report monazite Th-Pb ages from this sample as they are consistent with those from nearby specimens. For consistency, the results of analysis from each studied specimen are described from lower to higher structural level throughout this contribution; tables and figures follow the same pattern.

3. Analytical Methods

3.1. Petrological analysis

Petrographic observations of rock specimens used during this study were carried out primarily using an optical microscope. To assist with our investigations, Qualitative Evaluation of Materials by Scanning Electron Microscopy (QEMSCAN) maps of each thin section were used to aid in mineral identification, petrographic interpretations and calculation of phase modal proportion. Mineral abbreviations follow Whitney and Evans (2010) throughout.

Whole rock bulk compositions for selected specimens were obtained using a PANalytical 2404 X-ray fluorescence (XRF) vacuum spectrometer, equipped with a 4kW

Rh super sharp X-ray tube, housed at the X-ray Laboratory, Franklin and Marshall College, Pennsylvania, USA. Major element compositions were measured from a fused glass disc prepared by heating and quenching a mixture of 0.4 gm pulverized rock and 3.6 gm lithium tetraborate. The major element compositions are reported as oxide weight percent for SiO_2, Al_2O_3, CaO, K_2O, P_2O_5, TiO_2, $Fe_2O_3^T$, MnO, Na_2O and MgO.

3.2. Mineral Chemistry

Major element thin section maps and compositions of selected mineral phases were obtained in-situ using a CAMECA SXFive FE electron microprobe (EMP) housed in the Fipke Laboratory for Trace Element Research (FiLTER) facility at the University of British Columbia, Okanagan. Qualitative elemental maps of thin sections were prepared using the following analytical settings: 15 kV accelerating voltage, 200 nA beam current, 20 µm beam size, 20 µm step size and a dwell time of 15 ms in wavelength dispersive spectroscopy (WDS) mode. These maps were processed using ImageJ software for petrographic analysis including identification of mineral phases and their textural relationships. Quantitative spot analysis of garnet, feldspar, biotite, and muscovite were carried out in WDS mode using a 15 kV accelerating voltage, 20 nA beam current, 1 µm beam size with dwell time of 30ms on peak and 15ms on background. Oxides and mineral mounts of Smithsonian reference materials from CF Minerals and Micro Analytic Consultants were used as calibration standards. Compositional data from minerals were converted to atoms per formula unit (a.p.f.u) to derive mineral endmember compositions and ratios, which were used for thermodynamic calculations and phase equilibria modelling. Garnet compositions are reported as percentage of end members almandine (Alm) = $Fe^{2+}/(Fe^{2+}+Mg+Ca+Mn)$, pyrope (Prp) = $Mg/(Fe^{2+}+Mg+Ca+Mn)$, grossular (Grs) = $Ca/(Fe^{2+}+Mg+Ca+Mn)$ and spessartine (Sps) = $Mn/(Fe^{2+}+Mg+Ca+Mn)$. Feldspar compositions are reported as percentage of end members anorthite (An) = Ca/(Na+Ca+K), albite (Ab) = Na/(Na+Ca+K) and orthoclase (Or) = K/(Na+Ca+K). The Mg number in biotite, muscovite and garnet are reported as Mg# = $Mg/(Fe^{2+}+Mg)$.

Concentrations of selected trace element compostion including rare earth elements (REEs) and Y in garnet were acquired *in situ* using a ThermoScientific Element

XR inductively coupled plasma mass spectrometer (ICP-MS) coupled with a Photon Machines Analyte 193nm Excimer laser ablation system also housed in the FiLTER facility. Spot analyses were carried out using a laser beam diameter of ~ 29.6 µm with a fluence of ~ 6.67 J cm^{-2} and repetition rate of 8 Hz in continuous mode. NIST SRM 612 glass (with reference values from Pearce et al., 1997) was used as an external standard whereas the SiO_2 concentration measured by EMP analysis of the same garnet was used for internal calibration. Raw data were processed using the GLITTER software package (v. 4.2; Macquarie University, Australia) to derive trace element compositions. Where necessary, these compositions were normalized to the chondritic values using concentrations of McDonough & Sun (1995). Normalized Gd/Yb ratios are reported as $(Gd/Yb)_N$, whereas Eu anomaly is expressed as $(Eu/Eu^*)_N = (Eu)_N/[(Sm)_N \times (Gd)_N]^{0.5}$, where N marks normalization to the composition of CI chondrite from McDonough & Sun (1995). Monazite trace element composition was acquired simultaneously with isotope ratios during petrochronologic analysis. They are reported together with the geochronologic data presented below.

3.3. Phase equilibria modelling

Phase equilibria calculations were carried out using the Theriak-Domino program (v. 2012.01.03; de Capitani & Brown, 1987; de Capitani & Petrakakis, 2010) in an 11-component MnO - Na_2O - CaO - K_2O - FeO - MgO - Al_2O_3 - SiO_2 - H_2O - TiO_2 - Fe_2O_3 (MnNCKFMASHTO) system with the internally consistent HP98 (tc-ds55; Holland & Powell, 1998; updated 2004) thermodynamic dataset. Solid solution models used for this study include garnet and biotite (Mn-bearing model, Tinkham et al., 2001; White et al., 2005), plagioclase and K-feldspar (Holland & Powell, 2003), muscovite (Coggan & Holland, 2002), chlorite (Mn-bearing model, Holland & Powell, 1998; Mahar et al., 1997; Tinkham et al., 2001), magnetite-spinel (White et al., 2000, 2005), ilmenite (White et al., 2005), staurolite, cordierite, chloritoid, talc and epidote (Holland & Powell, 1998), and silicate melt (White et al., 2007). Quartz, kyanite, sillimanite, andalusite, rutile, and H_2O are modelled as pure phases.

Whole rock major element oxide abundances, obtained from XRF, combined with calculated H_2O were converted to Theriak Domino input and used for the construction of the phase diagrams. The subsolidus region is modelled in fluid saturated conditions with H_2O in excess, whereas the suprasolidus regions are modelled with iteratively calculated H_2O, enough to saturate the solidus, such that the fields in the suprasolidus region are fluid free (e.g. Johnson et al., 2008; Shrestha et al., 2017; White & Powell, 2002; White et al., 2005). With this approach, phase diagrams for structurally lower specimens 502074 and 502071, which do not record any evidence of anatexis, are calculated under fluid saturated subsolidus conditions whereas structurally higher specimens (502068, 502067, 502050 and 502056) that do record some textures indicative of partial melting are calculated under both fluid free suprasolidus conditions and saturated subsolidus conditions.

Because muscovite, biotite and plagioclase are generally prone to retrogression and recrystallization during retrograde conditions, the P-T estimates and P-T paths are primarily informed using the measured compositions of garnet grains. However, where appropriate, compositions from plagioclase and biotite are also used to provide information on the retrograde path for high-grade specimens. As the Ca content of the garnet is the least diffusive at high temperature (Vielzeuf et al., 2007), grossular is used as a primary isopleth to constrain P-T conditions, whereas the isopleth of Mg# for garnet is taken as secondary isopleth to account for almandine and pyrope content together. The P-T paths are inferred based on the intersections of these isopleths, with compositions taken from texturally and chemically defined locations along the garnet profiles, supported by the composition and textural locations of other minerals.

To account for increase in modal proportion of garnet during prograde growth, only the portion of the P-T path that crosses increasing garnet isomodes, calculated by phase equilibria modelling, is interpreted to represent the preserved prograde record and is used to constrain the prograde evolution of the rock. For the rocks that only experienced a subsolidus evolution, the retrograde portion of the path obtained from the diffused outer rim is used to provide information on the possible retrograde evolution, whereas for the rocks that experienced suprasolidus evolution with anatexis, the retrograde path ends with the solidification of melt. This approach is implemented because the absence of fluid after melt crystallization would inhibit any significant exchange reaction under subsolidus P-T conditions (Guilmette et al., 2011), thereby limiting the chances of resetting of chemical equilibrium. Moreover, along the retrograde path, the decoupling of faster- diffusing elements like Fe and Mg that may continue to equilibrate after slower diffusing elements like Ca have stopped doing so, can result in meaningless retrograde P-T paths if the paths are inferred based on the composition of the retrogressed garnet rim (Frost & Chacko, 1989; Kohn & Spear, 2000; Pattison & Begin, 1994; Spear, 1993). For this reason, for specimens that record only retrograde paths, the intersection of isopleths of garnet from the inner rim, which has not been affected by late retrograde diffusion, is used to infer the end of the P-T path. All P-T estimates from the phase diagrams are reported with uncertainties of ± 0.5 kbar on pressures and ± 25 ºC on temperatures, consistent with estimated uncertainties for this kind of modelling approach (e.g. Palin et al., 2016).

3.4. Quartz in garnet (QuiG) barometry

Quartz in Garnet (QuiG) barometry using laser Raman spectroscopy (Ashley et al., 2014a, 2016; Enami et al., 2007; Kohn, 2014b) was implemented to estimate the maximum pressure of entrapment (formation pressures) of quartz inclusions during garnet growth. A Renishaw Invia Basis Raman Microscope housed at the Institute for Scientific and Technological Research of San Luis Potosi (IPICYT), Mexico, equipped with a 633 nm Nd Laser, CCD detector, and confocal microscope with 1800 mm/lines grating was used to measure the frequency shift in the Raman spectrum of quartz inclusions during 11 sessions spanning 50 days. A 100X confocal objective with pinhole diameter of 25 μm was utilized for all of the analyses giving a spatial resolution of 1μm and spectral resolution of < 0.1 cm^{-1}. The room temperature was maintained at 21 ± 1 ºC. The majority of the spectra were collected on garnet grain mounts using six accumulations of 10 s each while the accumulations were doubled to twelve for the inclusions that yielded low counts. Herkimer quartz was used as the external standard while matrix quartz from a thin section of same specimen was used as the internal standard; both were measured multiple times throughout the session. The measured shift in the 464 cm^{-1} Raman spectrum peaks from the quartz inclusions relative to matrix quartz was used for the pressure calculation. Calculations of formation pressures were carried out with the QuIB Calc v 2.0 MATLAB program (Ashley et al., 2014b). This program takes the Raman shift as an input for the residual pressure calculation using a second order polynomial regression based on data of Schmidt and Ziemann (2000) (Ashley et al., 2014b). Further, based on the composition of the garnet, the estimated temperature, and the elastic model selected, it calculates the pressure of formation for the quartz inclusions in garnet from the residual pressures (see Ashley et al., 2014b for details). The elastic model of Guiraud and Powell (2006) was used for this study.

Quartz inclusions in garnet from selected specimens were used to calculate the formation pressure of the garnet from those specimens. No suitable quartz inclusions were identified in specimens below the MCT. At least thirteen inclusions in six garnet grains were measured from each specimen. Inclusions with visible impurities and along cracks in garnet were not considered. To compare with pressure estimates obtained through phase equilibria modelling, garnet compositions that yielded the peak pressure in phase diagrams and the associated temperature were used as an input to the ‘QuIB program’ for each specimen to calculate the formation pressures of the garnet. Because the location of a quartz inclusion relative to the garnet core, mantle, and rim was not discernable in the grain mounts, the results from quartz inclusions with the highest Raman shifts are reported here to provide estimates of maximum formation pressures for garnet from each specimen. Reanalysis of quartz inclusions from multiple days were within analytical uncertainties.

3.5. Monazite petrochronology

Monazite grains from selected specimens were analyzed in-situ using the Laser Ablation Split Stream (LASS) Multi Collector ICP-MS housed at the University of California, Santa Barbara. This approach allows simultaneous collection of isotopic and trace element data from the same spot. The LASS method used in this study follows Kylander-Clark et al. (2013), with the modifications of McKinney et al. (2015). Monazite grains were ablated using an 8 μm diameter spot at a 3 Hz repetition rate for 100 shots at a laser fluence of 1.5 J cm^{-2}, resulting in craters ~ 5 μm deep. Reference monazite ‘44069’ (424 Ma Pb/U ID-TIMS age, Aleinikoff et al., 2006) was used as the primary calibration standard for isotopic data, while ‘Bananeira’ (trace element values of Kylander-Clark et al., 2013) was used as the reference material for trace elements. In addition, ‘Bananeria’ and ‘FC-1’ were used as secondary monitors for isotopic data. Sixty-five repeat analyses of ‘Bananeira’ reference monazite yielded a weighted mean $^{206}Pb/^{238}U$ date of 508.5 ± 1.7, MSWD = 0.12 (508.9 Ma Pb/U LA-ICP-MS age, Kylander-Clark et al., 2013) while thirty-two analyses of monazite ‘FC-1’ returned a weighted mean $^{206}Pb/^{238}U$ date of 57.32 ± 0.25 Ma, MSWD = 0.29 (55.6 Ma ID-TIMS age, Horstwood et al., 2003), and a weighted mean $^{208}Pb/^{232}Th$ date of 54.80 ± 0.22, MSWD = 0.34 (54.5 ± 0.2 Ma LA-ICP-MS age; Kylander-Clark et al., 2013). Trace element concentrations are accurate to 3 - 5 % (2σ) based on the long-term reproducibility of multiple secondary reference minerals (Cottle et al., 2018).

3.6. Garnet geochronology

To investigate the timing of garnet growth and associated metamorphism, high-precision garnet Lu-Hf geochronology was carried out at the Pacific Centre for Isotopic and Geochemical Research, Department of Earth, Ocean and Atmospheric Sciences, University of British Columbia in Vancouver, following methods adopted from Smit et al. (2010). Multiple aliquots of garnet separates and a whole rock fraction from each of the selected specimens were analyzed to measure isotopic compositions of Lu and Hf. External reproducibility of $^{176}Hf/^{177}Hf$ was estimated based on repeated analyses of ATI - 475, an in-house reference material that was made from, and is isotopically identical to, the original Hf metal ingots from which JMC - 475 was developed ($^{176}Hf/^{177}Hf$ = 0.282160; Blichert-Toft & Albarède, 1997), at concentrations bracketing those of the samples. The external reproducibility was 41 ppm during the course of our analytical sessions. Total procedural blanks were 8 -15 pg Hf. Isochron dates and uncertainties were calculated using Isoplot v. 3.27 (Ludwig, 2003) with $\lambda^{176}Lu = 1.867 \times 10^{-11}$ yr^{-1} (Scherer et al., 2001; Söderlund et al., 2004).

4. Petrography and mineral chemistry

4.1. Metamorphic zonation

A description of the petrographic observations and observed mineral assemblage for selected specimens primarily used for thermobarometry are provided in Table 1 and 2 respectively, and are depicted in Figures 2 and 3. Based on observed mineral assemblages, petrography, field observations and published lithological descriptions of rocks from the HMC in the Modi Khola region, the study area has been divided into four metamorphic zones (Fig. 1).

<u>Garnet Zone I</u>

This zone includes phyllite and schist interbedded with quartzite and calc-silicate rocks from the Lesser Himalayan Sequence. The upper boundary of this zone is marked by the MCT (Fig. 1). The mineral assemblage in metapelite is predominantly Qz + Ms ± Pl ± Bt ± Grt ± Chl with accessory Ap ± Tur ± Zr ± Ilm ± Aln ± Mag. Biotite and muscovite define the primary foliation whereas garnet shows spiral inclusions with preserved growth zoning (see also Martin, 2009). No evidence of leucosome or anatexis has been reported from this zone (Martin et al., 2010; Corrie & Kohn, 2011).

<u>Garnet Zone II</u>

Garnet Zone II rocks form the lower portion of Greater Himalayan Sequence Unit I (Unit 1a; Corrie & Kohn, 2011) (Fig. 1). This zone primarily consists of schist and gneiss interbedded with quartzite. These rocks are locally migmatitic (Corrie & Kohn, 2011), which distinguishes them from those of Garnet Zone I. Pelitic rocks from this zone are characterized by the mineral assemblage Qz + Pl + Bt + Ms ± Grt with accessory Ap ± Tur ± Zr ± Rt ± Ep. Garnet in this zone preserves growth/oscillatory zoning of major elements plus near-rim increases in Mn, indicating a component of retrograde resorption (Corrie & Kohn, 2011; Kohn & Spear, 2000).

<u>Kyanite Zone</u>

This zone includes rocks from the middle portion of Greater Himalayan Sequence Unit I (Unit 1b; Corrie & Kohn, 2011) and is marked by the presence of kyanite in schist and gneiss (Fig. 1). The pelitic rocks in this zone are migmatitic and contain an assemblage of Qz + Pl + Bt ± Ms ± Grt ± Ky with accessory Ap ± Mnz ±Tur ± Zr ± Rt ± Xtm ± Ep (Corrie & Kohn, 2011). Preferentially oriented biotite and muscovite define the foliation and garnet major element profiles are nearly homogeneous, consistent with high temperature diffusion (Kohn & Spear, 2000). Garnet rims locally record an increase of Mn at the rims, indicating minor resorption during retrograde metamorphism (Corrie & Kohn, 2011; Kohn & Spear, 2000)

<u>Garnet Zone III</u>

The rocks of Garnet Zone III include those from the upper portion of Greater Himalayan Sequence Unit I (Unit 1c; Corrie & Kohn, 2011), Unit II and Unit III and primarily consists of schist and gneiss with calc-silicate, marble and quartzite in the upper portion (Fig. 1). The mineral assemblage of Garnet Zone III is commonly Qz + Pl + Bt ± Ms ± Grt ± Hbl with accessory Kfs ± Sil ± Cal ± Cpx ± Ap ± Mnz ± Ep ± Ttn ± Chl. These rocks record significant anatexis and migmatization including segregated leucosomes. While sillimanite has been reported in this zone, it has been interpreted as metasomatic and not part of the primary metamorphic assemblage (Corrie & Kohn, 2011). Garnet in this zone has homogenous cores and near-rim increases in Mn, indicating high temperature diffusion and later retrograde resorption (Corrie & Kohn, 2011; Kohn & Spear, 2000).

4.2. Major element chemistry

Major metamorphic minerals including garnet, biotite, muscovite and plagioclase were analyzed for major element concentrations. Representative mineral compositions for selected specimen are presented in Table S1.

4.2.1. Garnet

All garnet grains analyzed for this study primarily have an almandine composition (Table S1). Representative garnet profiles are presented in Figure 4, with the profiles of other analyzed garnet grains reported in Figure S1. Garnet chemistry is discussed below from low to high structural levels. Garnet from specimen 502074 (Fig. 1) have a composition of Alm_{66-75} Prp_{6-11} Grs_{12-24} Sps_{0-4} ($Mg\#_{0.08-0.12}$), which show typical prograde zoning (e.g. Tracy et al., 1976; Woodsworth, 1977); a core with high grossular and spessartine that progressively decreases towards the rim (Grs_{23} Sps_4 to Grs_{12} Sps_0) compensated by an increase in almandine and pyrope (Alm_{66} Prp_6 to Alm_{75} Prp_{11}) (Fig. 4a). Garnet grains from specimen 502071 (Fig. 1) have compositions of Alm_{67-77} Prp_{7-11} Grs_{11-18} Sps_{1-7} ($Mg\#_{0.09-0.13}$) and record similar prograde zoning to that observed in specimen 502074 with decreasing grossular and spessartine toward the rim (Grs_{18} Sps_7 to Grs_{11} Sps_1) concomitant with an increase in almandine and pyrope (Alm_{67} Prp_7 to Alm_{77} Prp_{11}) (Fig. 4b). A small increase in spessartine (Sps_2) is observed at the outer rim of one of the grains compensated by a decrease in pyrope (Prp_9). Garnet grains from specimen 502068 (Fig. 1) have compositions of Alm_{64-67} Prp_{10-16} Grs_{12-15} Sps_{3-8} ($Mg\#_{0.12-0.20}$). Most of the grains have almost homogeneous core compositions with only one garnet recording a minor progressive decrease in spessartine towards the rim (Sps_5 to Sps_4) compensated by an increase in almandine (Alm_{64} to Alm_{67}) (Fig. 4c). The outer rims of all garnet grains show a sharp increase in spessartine and decrease in pyrope (Prp_{15} Sps_4 to Prp_{11} Sps_6). The composition of garnet grains in specimen 502067 (Fig. 1) range between Alm_{67-75} Prp_{13-25} Grs_{3-5} Sps_{3-7} ($Mg\#_{0.14-0.27}$) and have homogeneous cores (Alm_{67-68} Prp_{23-25} Grs_{3-5} Sps_{3-4}) with a very minor rim-ward decrease in spessartine recorded in one of the garnet grains (Fig. 4d). Garnet rims in all the investigated grains are characterized by a significant decrease in pyrope (Prp_{13}) compensated by increase in almandine and spessartine (Alm_{75} and Sps_7). The composition of garnet grains in specimen 502050 (Fig. 1) range between Alm_{71-77} Prp_{13-20} Grs_{4-6} Sps_{3-5} ($Mg\#_{0.14-0.22}$). Compositional profiles from four grains show homogenous cores and mantle domains with rims that record an increase in almandine (Alm_{72} to Alm_{77}) and decrease in pyrope (Prp_{19} to Prp_{13}) (Fig. 4e). Grossular and spessartine are almost constant throughout with very minor decreases in spessartine observed at the outer rims. Garnet grains from specimen 502056 (Fig. 1) have compositions in the range of Alm_{56-69} Prp_{7-11} Grs_{8-24} Sps_{9-16} ($Mg\#_{0.09-0.14}$). The larger grain shows a complex elemental profile defining a core, mantle, inner rim and outer rim domains. The homogeneous core (Alm_{64-66} Prp_{9-11} Grs_{11-13} Sps_{11-13}) displays a slight decrease in spessartine outward (Fig. 4f). The mantle is characterized by a sharp increase in grossular compensated by a sharp decrease in almandine and pyrope (Alm_{56} Prp_8 Grs_{24}). The inner rim shows a gradual increase in almandine and pyrope and decrease in grossular and spessartine (Alm_{65} Prp_{10} Grs_{13} Sps_{10}), whereas the outer rim records a distinct increase in spessartine correlated to a decrease in pyrope (Prp_7 Sps_{16}). The smaller garnet grain shows a profile that matches the pattern of the mantle to outer rim of the larger grain (Fig. S1), perhaps reflecting a profile measured across a non-equatorial section.

4.2.2. Biotite

Biotite grains from all specimens are annite in composition (Table S1). Grains analyzed in specimen 502074 range in Mg# between 0.49 and 0.58 and in Ti content between 0.11 and 0.18 a.p.f.u.; no systematic spatial trend is observed (Fig. 5a). In specimens 502071 and 502068, biotite has Mg# of 0.37 - 0.43 and 0.46 - 0.50, respectively, and Ti contents of 0.16 - 0.32 and 0.16 - 0.27 a.p.f.u., respectively (Fig. 5b, c). There is a weak textural trend for Ti content, where matrix grains have higher Ti contents than those near or included within garnet in both specimens. Specimen 502067 has biotite with high Mg# in the range 0.52 - 0.73, and a large spread in Ti content, between 0.07 - 0.31 a.p.f.u., (Fig. 5d). Biotite inclusions in garnet show higher Mg# (0.64 - 0.73) and lower Ti content (0.07 - 0.15 a.p.f.u), whereas matrix biotite grains have higher Ti content (0.16 - 0.22 a.p.f.u) (Fig. 5d). Biotite grains in specimen 502050 show Mg# in range of 0.46 - 0.53 and Ti contents of 0.10 - 0.37 (Fig. 5e), but do not show any textural variation. For specimen 502056, Mg# in biotite ranges between 0.29 and 0.41, whereas Ti content shows a large spread between 0.19 and 0.53 a.p.f.u (Fig. 5f). Biotite grains in the matrix have slightly higher Mg# (0.36 - 0.41) compared to other grains. A single analysis from a biotite grain included in garnet in specimen 502056 (not shown in Fig. 5f) has a lower Mg# and Ti content (0.28, 0.15 a.p.f.u) compared to other grains.

All muscovite grains analyzed during this study show similar compositions in Si contents ranging between 6.08 and 6.33 a.p.f.u. without any correlation to spatial or textural setting (Table S1). Two analyses from muscovite grains included in garnet in specimen 502056, however, have higher Si contents (6.59 and 6.62 a.p.f.u). Muscovite in specimen 502074 shows the highest Mg# of all specimens, ranging between 0.59 and

0.67, whereas Mg# in specimens 502071, 502068 and 502050 are similar, and show a spread between 0.39 and 0.55, 0.35 and 0.50, and 0.37 and 0.52, respectively. Finally, muscovite in specimen 502067 shows intermediate Mg# that varies between 0.47 and 0.64 with no systematic trend.

4.2.3. Feldspar

All specimens examined contain plagioclase. Plagioclase in specimen 502074 has an anorthite content of An_{18-31}, which is systematically higher in the matrix (An_{27-31}) compared to that near garnet (An_{18-26}). Plagioclase compositions in specimens 502071 and 502068 have variable anorthite contents of An_{10-16} and An_{19-27}, respectively, with no trend related to textural position. The anorthite content of plagioclase in specimen 502067 ranges between An_{11-14} without any spatial trend. Plagioclase in specimen 502050 has anorthite content of An_{15-21} with relatively low anorthite contents (An_{15-18}) in grains that are in the matrix compared to those near garnet (An_{16-21}). The structurally highest specimen, 502056, is the only rock analysed that contains both plagioclase and K-feldspar. Plagioclase has an anorthite content of An_{21-27}, with grains included in garnet having a higher anorthite components (An_{24-27}) compared to those in the matrix and near garnet. All K-feldspar grains in specimen 502056 were measured in the matrix and have an orthoclase content of Or_{88-91}.

4.3. Trace element chemistry

Garnet grains from selected specimens were analyzed for selected trace element concentrations including rare earth elements (REEs) and Y (Table S2). Trace element profiles and chondrite normalized REE ratios from the grains analyzed in each specimen are presented in Figures 6 and S2. Garnet grains from specimen 502074 show a zoned profile for REEs and Y. Garnet cores have relatively high Lu (up to ~ 10 ppm) and low Y (as low as ~ 50 ppm), along with low $(Gd/Yb)_N$ values (~ 0.02) and a negative Eu anomaly (~ 0.4 - 0.7). The Lu content gradually decreases towards the rims (~ 2 ppm) before increasing in the outer rims (~ 8 ppm), whereas Y content progressively increases towards the rims (~ 250 ppm) (Figs 6a and S2). While there is no distinct change in Eu anomaly, $(Gd/Yb)_N$ values increase towards the rims (~ 0.23), indicating significant enrichment in MREE compared to HREE.

Garnet grains from specimen 502071, which show similar prograde zoning profiles for the major elements, show different trace element profiles (Figs 6b and S2). The trace element profile from one of the analyzed garnet grains shows a bowl-shaped profile with low Lu (~ 0.5 ppm) and low Y (~ 144 ppm) in the core that gradually increases towards the rim (up to ~ 28 ppm Lu and ~ 952 ppm Y). A significant decrease in Lu (down to ~ 2 ppm) is observed in the outer rims. The core of the garnet also records high $(Gd/Yb)_N$ values (~ 1.05) that decrease sharply towards the rims (to ~ 0.02), indicating enrichment in HREE towards the rim (Fig. 6b). The Eu anomaly becomes increasingly more negative outward from the core (~ 0.9) towards the rim (~ 0.4). The profile from the other garnet shows scattered Lu and Y content with no discernable zonation (Fig. S2). $(Gd/Yb)_N$ values and Eu anomalies also do not show any trend from core to rim. However, the concentrations of HREE and Y were significantly higher (Lu ~ 12 - 76 ppm and Y ~ 537 - 1439 ppm) than in the other garnet analyzed (Figs 6b and S2). Garnet grains in specimen 502068 display trace-element zoning (Figs 6c and S2). Garnet cores are relatively enriched in HREE with high Lu (~ 15 - 25 ppm) and Y (~ 600 - 1000 ppm). In addition, cores also record low $(Gd/Yb)_N$ values (< 0.05) and have moderate negative Eu anomalies (0.5 - 0.7). Both Lu and Y gradually decrease outwards to rims depleted in HREE (Lu ~ 1 - 5 ppm; Y ~ 200 ppm). While the $(Gd/Yb)_N$ ratio in one of the grains shows a significant increase toward the rims (up to ~ 0.6), the ratio is constant in the other grain (Figs 6c and S2). The Eu anomalies are largely similar with a minor decrease in negative Eu anomaly at the rims (~ 0.9).

Garnet grains in specimen 502067 show weak zonation in trace elements (Figs 6d and S2). Profiles show cores that are relatively high in Lu (~ 20 - 30 ppm) and Y (up to 500 ppm), with a mostly negative Eu anomaly (~ 0.7 - 1.0). Lutetium in both grains shows a gradual decrease towards rims (~ 2 - 10 ppm) and a sharp asymmetric increase (~ 22 - 23 ppm) at one side of the grain. Yttrium decreases towards rims (~ 150 - 300 ppm) except for the outer rim of one garnet grains that records a significant increase in Y content on one side (up to 488 ppm). $(Gd/Yb)_N$ values are relatively low (~ 0.01 - 0.15) and do not show any systematic trend. Although there is no well-organized pattern, the outer rims generally have a larger negative Eu anomaly (~ 0.5) compared to the cores (~ 0.8) (Figs 6d and S2). Garnet grains from specimen 502050 show almost invariant concentrations of trace elements except at the rims (Figs 6e and S2). A profile across one garnet grain shows relatively minor increases of Lu (~ 1.8 to 7 ppm) and Y (~ 148 to 265 ppm) outwards from core to rim (Fig. 6e), whereas a profile across a second garnet grain shows a homogeneous core with significant decreases in Lu (from ~ 9 to 2 ppm) and Y (from ~ 258 to 150 ppm) at the inner rim and sharp increases at the outer rim (Lu ~ 8 ppm; Y ~ 226 ppm) (Fig. S2). With the exception of two analyses from the core of the first garnet (Eu anomaly of 1.6 and 2.9), the Eu anomaly is primarily negative (~ 0.4 - 0.9) without any spatial pattern. $(Gd/Yb)_N$ values also do not show any trend and are flat except at one side of one garnet grain, where they show a sharp increase (from ~ 0.05 to 0.35) at the inner rim before dropping (~ 0.05) at the outer rim (Figs 6e and S2).

Similar to the garnet major element profiles in specimen 502056, trace element concentrations in garnet grains examined in this specimen show complex zonation (Figs 6f and S2). The core from the larger garnet grain shows depleted HREE with low Lu (~ 20 - 40), low Y (~1200 ppm) and high $(Gd/Yb)_N$ value (~ 0.05 - 0.09), whereas the mantle is characterized by increasing Lu (up to 149 ppm) and Y (up to 2331 ppm) with significant enrichment in HREE compared to MREE, and records the lowest $(Gd/Yb)_N$ values (~ 0.02). The inner rim of the same grain shows decreasing Lu (down to ~ 26 ppm) and Y (~ 1230 ppm) with an increase in $(Gd/Yb)_N$ values (up to ~ 0.12) indicating depletion of HREE towards rims (Fig. 6f). Minor increases in Lu and Y are also observed at the outermost rim, also reflected as a small decrease in $(Gd/Yb)_N$ values. The smaller grain follows the pattern of the mantle to the rim of the larger grain (Fig. S2). The negative Eu anomaly decreases towards the mantle (from 0.2 up to 0.5) in the large grain and then increases towards the rims (down to 0.15), which is also evident on the smaller grain (Figs 6f and S2).

5. Thermobarometry

5.1. Phase diagrams and P-T paths

Major element bulk composition of selected specimens used for phase equilibria modelling and the Theriak Domino input are presented in Table 3 and 4 respectively.

The intersections of garnet inner rim isopleths from all specimen plot at or near the intersections of ± 1 % modal envelope for the observed mineral assemblages (Fig. S3), indicating that garnet inner rims and the observed mineral assemblage likely equilibrated together (Guilmette et al., 2011). As such, the intersections from garnet inner rim end-member compositions, along with measured modal isopleths, are used to provide a minimum estimate for P-T conditions at which the specimen was still in equilibrium during or after peak P-T conditions (Guilmette et al., 2011; Palin et al., 2016). Isopleths from the outermost rims of garnet in most specimens that experienced anatexis intersect at lower P-T across the solidus in water saturated supra-solidus fields. In the absence of any evidence to indicate influx of fluid during retrogression, such intersections obtained from the outermost rims are only used to infer probable retrograde paths, and as such are not discussed in detail.

5.1.1. Specimen 502074

The observed peak assemblage of Qz + Pl + Grt + Bt + Ms + Chl + Ilm in specimen 502074 covers a broad P-T field of ~ 4.3 - 7.7 kbar and 555 - 595 ºC (Fig. 7a). Modal isopleths intersect at ~ 6.3 - 7.3 kbar and 575 - 600 ºC within the field of the observed assemblage (black stippled box, Figs 7a, b and S3). The intersections of garnet rim end member isopleths plot in the same field and overlap the modal envelope, consistent with the preservation of the final assemblage. Garnet core compositions for this specimen intersect within a low-temperature biotite-absent assemblage at ~ 6.5 kbar and 545 ºC, whereas inner rim isopleth compositions intersect at similar pressure but higher temperature at ~ 6.6 kbar and 575 ºC, defining the peak P-T estimate for this specimen (Fig. 7b). The outer rim isopleths intersect at similar temperature to those from the inner rim but at slightly lower pressure at ~ 6.2 kbar and 580 ºC. The inferred P-T path is thus a prograde heating path followed by late decompression and cooling (Fig. 7b). This clockwise P-T path is consistent with the absence of staurolite in the assemblage as a temperature increase would take the path into the staurolite-bearing field.

5.1.2. Specimen 502071

The phase diagram for specimen 502071 indicates a high-pressure evolution with the observed assemblage of Qz + Pl + Grt + Bt + Ms + Ilm stable up to ~ 11.4 kbar across a temperature range of ~ 560 to 660 ºC in the given P-T range, just below the solidus (Fig. 8a). Modal isopleths for this rock intersect at ~ 9.5 - 10.5 kbar and 630 - 655 ºC, within the observed assemblage (black stippled box, Figs 8a, b and S3), and overlap the intersection of garnet rim compositions, indicating preservation of the final assemblage. These P-T conditions are also consistent with the absence of anatexis in the specimen. Garnet core isopleths plot in a high-pressure paragonite-present assemblage at ~ 11.4 kbar and 600 ºC whereas inner rim isopleths plot at a lower pressure of ~ 10.3 kbar and higher temperature of ~ 635 ºC (Fig. 8b), which provides the estimate for peak T experienced by this rock. The zonation in garnet is compatible with a minor increase in temperature during crystallization of the inner rim. The outer rim plots at lower pressure ~ 8.5 kbar and temperature ~ 620 ºC (Fig. 8b), consistent with minor retrogression observed at outer rims in garnet, which is replaced by biotite. The interpreted P-T path for this specimen is, thus, a clockwise decompressional path with initial heating followed by late cooling (Fig. 8b).

5.1.3. Specimen 502068

A similar high-pressure evolution is also interpreted from the phase diagram for specimen 502068. The preserved peak assemblage of Qz + Pl + Grt + Bt + Ms + Rt + Melt covers a wide P-T field at ~ 8 to > 12 kbar (outside the P-T range shown) and ~ 670 to > 750 ºC, in the suprasolidus region (Fig. 8c). The modal isopleths for this rock (black stippled box, Figs 8c, d and S3) intersect at ~ 8.8 - 9.8 kbar and 640 - 665 ºC and overlap the solidus, consistent with the rock crystallizing at the solidus on a return path (Indares et al., 2008). Garnet core isopleths cross at ~ 11.3 kbar and 675 ºC, marking the minimum estimate for the peak P-T experienced by this specimen. The inner rim composition indicates a decrease in pressure and temperature and plots near the modal envelope within analytical uncertainties of phase equilibria modelling (Palin et al., 2016) and at the solidus at ~ 10.2 kbar and 660 ºC, consistent with retrogression marked by an increase in spessartine towards the rims. The compositions of garnet outer rims plot at lower P-T conditions of ~ 8.8 kbar and 610 ºC (Fig. 8d), however, this intersection is only used as a reference to infer a late stage retrograde path as discussed above. The interpreted P-T path for this specimen is clockwise decompression and cooling with an equilibration of the observed assemblage at the solidus.

5.1.4. Specimen 502067

Kyanite-bearing specimen 502067 shows a decompressional path similar to that of specimen 502068. The muscovite-absent preserved peak assemblage of Qz + Pl + Grt + Bt + Ky + Rt + Melt covers a wide P-T field beside the solidus extending from ~ 7.1 kbar to >11 kbar (outside the P-T range shown) and ~ 660 ºC to > 750 ºC (Fig. 9a). The modal isopleths intersect in the observed assemblage across the solidus at ~ 7.2 - 8.2 kbar and 645 - 670 ºC (black stippled box, Figs 9a, b and S3). Minimum estimates for peak P-T conditions are obtained from the homogeneous core compositions of garnet, which plot at ~ 8.7 kbar and 675 ºC (Fig. 9b). The inner rim isopleths plot at lower pressure within the modal envelope near the solidus at ~ 7.9 kbar and 665 ºC, yielding a P-T estimate for crystallization of the observed assemblage on the retrograde path. The retrogressed rim compositions observed in the garnet profiles plot at P-T conditions of ~ 6.2 kbar and 610 ºC. The interpreted P-T path outlines a clockwise decompressional cooling path (Fig. 9b) with final crystallization at the solidus. The presence of minor muscovite in this specimen indicates late crystallization along the retrograde path at low P-T as calculated by the phase diagram. (Fig. 9a, b).

5.1.5. Specimen 502050

Another kyanite-bearing specimen, 502050, also shows similar P-T evolution to that of specimen 502067 from the same structural panel (Fig. 1). The muscovite-present assemblage of Qz + Pl + Grt + Bt + Ms + Ky +Rt + Melt extends from ~ 7.8 kbar to > 10 kbar (outside the P-T range shown) and ~ 655 ºC to > 750 ºC (Fig. 9c). The modal isopleths for this specimen also plot within the observed assemblage and across the solidus at ~ 7.2 - 8.2 kbar and 645 - 670 ºC (black stippled box, Figs 9c, d and S3). The homogeneous core compositions of garnet plot at ~ 8.5 kbar and 680 ºC and provide a minimum estimate for the peak P-T experienced by the rock (Fig. 9d). The inner rim composition plots at slightly lower pressure within the modal envelope near the solidus, ~ 7.7 kbar and ~ 665 ºC, indicating melt crystallization along the retrograde path and outlines a clockwise decompression and cooling path similar to specimen 502067 (Fig. 9d). The outer rim compositions for this specimen also plot at lower P-T conditions of ~ 5.9 kbar and 615 ºC, similar to specimen 502067.

5.1.6. Specimen 502056

The structurally highest specimen, 502056, records a higher temperature evolution than the other rocks in this study, consistent with the preserved peak assemblage of Qz + Pl + Kfs + Grt + Bt + Ms + Rt/Ilm + Melt that occupies a P-T range of ~ 8.5 to > 12 kbar (outside the P-T range shown) and ~ 640 to > 765 ºC (Fig. 10a). The modal isopleths intersect within the observed equilibrium mineral assemblage at ~ 7.1 - 8.1 kbar and 675 - 700 ºC (black stippled box, Figs 10a, b and S3). The isopleths from the homogeneous core of the large garnet plot at ~ 8.7 kbar and ~ 700 ºC. The peak P-T calculated by phase equilibria modelling for this specimen comes from the composition taken from the outer cores of the large garnet and the core of small garnet, which plot at ~ 11.2 kbar and 695 ºC (Fig. 10b).

The outer rims of both grains plot near the solidus at ~ 6.2 kbar and 640 ºC, giving a P-T estimate for the equilibration of the rock as it crossed the solidus (Fig. 10b). Because the composition of the core from the larger grain is almost identical to the inner rim composition from both grains, and there is a sharp jump in chemical composition at the outer core of the large garnet, we argue that it either represents a relict core from pre-existing garnet or the profile represents a section that was cut through an irregular garnet. As such, only the path obtained from the smaller garnet and outer portion of large garnet are used to interpret the preserved metamorphic evolution. The interpreted P-T path is thus an isothermal decompression path with minor cooling (Fig. 10b), with final crystallization at the solidus.

5.2. Quartz inclusion formation pressure

The measured Raman shift of the 464 cm^{-1} quartz peaks from the inclusions in garnet varies throughout all the analyzed specimens (Table 5), but the overall average shows a greater peak shift in the specimens from the lower structural levels directly above the MCT. This indicates higher residual pressure and higher calculated formation pressures for the garnet from those specimens which are structurally lower compared to those above the Bhanuwa fault. The measured peak shifts in specimens 502071, 502069 and 502068, were 2.24 cm^{-1}, 2.85 cm^{-1} and 2.19 cm^{-1}, respectively, with calculated residual pressure of 2.47 kbar, 3.15 kbar and 2.41 kbar. When combined with the peak temperature of 600 ºC and 675 ºC obtained from phase equilibria modelling for each specimen, the residual pressures translate to formation pressures of 10.9 ± 0.3 kbar (502071) and 11.9 ± 0.2 kbar (502068). No phase equilibria modelling was carried out for specimen 502069. Using the temperature from the closest specimen, 502068 (from the same structural panel), the pressure for 502069 is estimated to be 13.1 ± 0.2 kbar. Calculated QuiG pressure estimates from these specimens are slightly higher but consistent with peak pressures of ~ 11.4 kbar and ~ 11.3 kbar obtained from phase equilibria calculations for specimen 502071 and 502068, respectively.

The maximum peak shifts measured in specimens 502067, 502050 and 502056 were 1.73 cm^{-1}, 1.70 cm^{-1} and 1.43 cm^{-1}, respectively, indicating residual inclusion pressures of 1.91 kbar, 1.87 kbar and 1.58 kbar. Using peak metamorphic temperatures of 675 ºC, 680 ºC and 695 ºC obtained from the phase equilibria modelling of these specimens, the calculated residual pressures translate to pressures of formation of 11.1 ± 0.3 kbar (502067), 11.2 ± 0.3 kbar (502050) and 11.0 ± 0.2 kbar (502056). The pressure obtained from quartz inclusions in garnet for specimen 502056 is consistent with the peak pressure of ~11.2 kbar from phase equilibria modelling. Quartz inclusion pressures in specimens 502050 and 502067, however, record significantly higher pressures than ~ 8.7 kbar and ~ 8.5 kbar calculated from phase equilibria modelling.

6. Monazite and garnet (petro)chronology

6.1. Monazite age and trace element data

Monazite grains analysed in all specimens were located in the matrix. Monazite age data from most of the specimens record semi-continuous to continuous Cenozoic dates, however, some spot analyses yield Precambrian or Mesozoic dates. These old dates likely reflect inherited (detrital) or mixed ages and are therefore excluded from further consideration (refer to complete U-Th/Pb data presented in Table S3). Because of the low natural abundance of ^{235}U and the existence of unsupported ^{230}Th in young monazite, such as those recording the Cenozoic metamorphism of the Himalaya, may result in imprecise U/Pb dates (Cottle et al., 2012; Schärer, 1984), the age data reported in this work refer the $^{232}Th/^{208}Pb$ system. Moreover, higher Th concentrations compared to U in monazite (often in weight %; Chang et al., 1996), and nearly 100 % natural abundance of ^{232}Th, makes the $^{232}Th/^{208}Pb$ date more suitable for this study.

Only one grain was possible for dating in the structurally lowest specimen examined, 502035. Out of four usable spot analyses, only one returned a Cenozoic $^{232}Th/^{208}Pb$ date, 10.2 ± 1.0 Ma (Fig. 11a). Because of the potential unsupported ^{206}Pb resulting from preferential uptake of ^{230}Th, the analysis plots as a reversely discordant date on the U-Th/Pb concordia diagram (Schärer, 1984). The trace element data from this spot record high Y concentration (16200 ppm). It also shows a medium $(Gd/Yb)_N$ value (76.1) and relatively low negative Eu anomaly (0.96), compared to trace element data from other specimens discussed below (Fig. 12).

Twenty-two total spot analyses carried out across four monazite grains in specimen 502073 yielded five Cenozoic dates, ranging from 38.1 ± 2.4 Ma to 13.02 ± 0.2 Ma (Fig. 11b). As with the previous specimen, the analyses plot as reversely discordant on the U-Th-Pb concordia diagram, indicating excess ^{206}Pb (Schärer, 1984). The oldest analysis yielded a very low Y concentration (1108 ppm), a medium $(Gd/Yb)_N$ value (59.7) and a weak negative Eu anomaly (0.95), whereas the younger analyses show relatively high Y contents (6840 - 11180 ppm), similar $(Gd/Yb)_N$ values (51.2 - 68.2) and slightly more pronounced negative Eu anomalies (0.69 - 0.71) (Fig. 12).

Twenty-two spots from five monazite grains in specimen 502072 returned nine Cenozoic dates with two distinct populations. The older population (n = 4) ranges from

53.0 ± 0.9 Ma to 41.4 ± 1.0 Ma, whereas the younger population (n = 5) ranges from 18.2 ± 0.8 to 6.6 ± 0.2 Ma (Fig. 11c). The older population has relatively consistent trace element compositions with low Y concentrations (1552 - 2070 ppm), very low $(Gd/Yb)_N$ values (7.0 - 27.8) and moderate negative Eu anomalies (0.51 - 0.67). The Y concentrations are markedly higher for the younger analyses (3670 - 30800) trending towards higher values with younger dates. The $(Gd/Yb)_N$ values are low to moderate for the younger population (32.5 - 150.3) and are negatively correlated with Y contents. The Eu anomalies in the younger analyses are weakly to moderately negative (0.51 - 0.91), with younger analysis showing the smallest anomalies (Fig. 12).

Eleven monazite grains were analyzed in specimen 502067. Ninety-seven out of 107 spots yielded Cenozoic; these range from 39.4 ± 1.4 Ma to 15.9 ± 0.5 Ma and show one major population at ca. 23.8 ± 0.1 Ma, MSWD = 0.4 (n = 19) (Fig. 11d). All analyses have moderate to high Y concentrations (7160 - 25550 ppm) with a weak trend of increasing Y with younger dates until ca. 18 Ma, after which Y begins to decrease slightly. The Eu anomalies across all analyses are moderately to weakly negative (0.55 - 0.93). The $(Gd/Yb)_N$ values are generally low to moderate (11.5 - 137.2, with one analysis at 25.4 Ma recording the highest value of 297.4). Analyses between ca. 39 and 25 Ma show relatively scattered $(Gd/Yb)_N$ values with a weak trend of increasing values towards younger dates, whereas the analyses between ca. 25 and 16 Ma show a systematic trend of decreasing values towards younger dates, with the dates between ca. 23 and 16 Ma characterized by the lowest values (Fig. 12).

All 164 spots from eight monazite grains in specimen 502050 returned Cenozoic dates, which range between 32.9 ± 1.0 Ma and 15.3 ± 0.8 Ma. The dates define two distinct populations at ca. 31.4 ± 0.2 Ma, MSWD = 0.7 (n = 77) and ca. 23.8 ± 0.1Ma, MSWD = 0.6 (n = 16) (Fig. 11e). The older population, between ca. 33 and 28 Ma, is characterized by low to medium Y concentrations (718 - 12400), relatively high $(Gd/Yb)_N$ values (75.0 - 1021.4, with one analysis at 31.9 Ma showing 1471.4) and relatively low to moderate negative Eu anomalies (0.64 - 0.90). The younger population is associated with moderate to high Y concentrations (2250 - 29900), relatively low $(Gd/Yb)_N$ values (51.56 - 815.6, mostly between 51.6 - 511.6) and similarly negative Eu anomalies (0.59 - 0.80) compared to the older population (Fig. 12). For both populations, date correlates negatively with Y concentration and positively with $(Gd/Yb)_N$ values.

One hundred and thirty-eight out of 140 spots yielded Cenozoic dates in specimen 502056; they range between 53.8 ± 3.3 Ma and 14.8 ± 0.4 Ma. Similar to the previous specimen, there are two distinct populations. An older population (> 40.7 ± 1.12 Ma, n=14) has a peak at ~ 43.2 ± 0.5 Ma, MSWD = 0.7 (n=6) and a younger population (< 24.5 ± 0.6 Ma, n = 124) has a peak at ~ 22.6 ± 0.1, MSWD = 0.9 (n = 62) (Fig. 11f). The older population is characterized by very low Y concentrations (520 - 1820 ppm), low to medium $(Gd/Yb)_N$ values (21.4 - 64.1) and strongly negative Eu anomalies (0.09 - 0.21) (Fig. 12). The Y concentrations are significantly higher for the younger population (8500 - 40500 ppm) and show a positive correlation with younger dates. Both $(Gd/Yb)_N$ values (12.0 - 77.4) and Eu anomalies (0.10 - 0.24) show similar values to those of the older population, with $(Gd/Yb)_N$ values increasing with younger spots and Eu anomalies decreasing slightly with younger dates (Fig. 12).

6.2. Garnet Lu-Hf analysis

All specimens analyzed yield well-defined garnet-whole rock isochrons (Table 6, Fig. 13). The structurally lowest specimen, 502074, yields the youngest garnet Lu-Hf date at 16.8 ± 0.5 Ma, MSWD = 1.3 (n = 5). Garnet geochronology for specimens 502071 and 502068 provided late Eocene dates of 34.0 ± 0.1 Ma, MSWD = 1.6 (n = 5) and 35.1 ± 0.2 Ma, MSWD = 1.1 (n = 5) respectively, whereas the Lu-Hf data from 502067 yielded a younger, late Oligocene date of 27.8 ± 0.2 Ma, MSWD = 1.7 (n = 4). The structurally highest specimen analyzed, 502056, returned a late Eocene date of 34.7 ± 0.1 Ma, MSWD = 1.9 (n = 4).

7. Interpretations

7.1. Trace element partitioning

Trace element compositions of minerals have been widely used to infer the growth and breakdown of co-existing mineral phases in metamorphic systems (e.g. Foster et al., 2002; 2004; Hermann & Rubatto, 2003; Larson et al., 2018; Pyle & Spear, 1999; Regis et al., 2014; Rubatto et al., 2006; Shrestha et al., 2019). In particular, trace element partitioning between major silicate minerals such as garnet and plagioclase, and accessory minerals such as monazite (LREE-phosphate), xenotime (Y-rich phosphate), allanite (REE silicate) and apatite (MREE-rich phosphate) has been used extensively to inform the relative/absolute timing of growth and/or breakdown of those minerals (e.g. Godet et al., 2020; Hermann & Rubatto, 2003; Larson et al., 2018; Rubatto et al., 2006, 2013; Shrestha et al., 2019; Soret et al., 2019). Moreover, because some trace elements are less prone to high temperature diffusion than major elements (Chernoff and Carlson, 1999; Otamendi et al., 2002), they may be able to provide useful information on the metamorphic history in specimens where major elements may have been homogenised.

The concentration of trace elements in minerals primarily depends on the total trace element budget available in the system during their growth, which may be available from a stock reservoir (e.g. enriched fluids or melts) or becomes available by breakdown of other phases that contains those elements (Otamendi et al., 2002; Raimondo et al., 2017). For example, REE growth zoning in garnet could reflect differential uptake of REEs either through Rayleigh fractionation, indicating rapid intragranular diffusion for REEs relative to crystal growth in equilibrium with the matrix (Hollister 1966; Otamendi et al., 2002; Raimondo et al., 2017), or reaction-controlled matrix equilibration, where REE supply is controlled by sequential garnet-forming mineral breakdown reactions (Konrad-Schmolke et al., 2008; Pyle & Spear, 2003; Raimondo et al., 2017). While growth zoning with Rayleigh fractionation would result in smooth core-to rim variation of elements with bell shaped profiles, growth zoning under reaction-controlled matrix equilibration may be marked by a transition from bell- to bowl-shaped profiles with decreasing atomic number (Raimondo et al., 2017). These fluctuations in the supply of available trace elements and their fractionation during mineral growth can produce distinct changes in trace element compositions of the mineral at different P-T conditions, which can be used as an indicator of metamorphic process (Spear & Pyle, 2002). In the following paragraphs, trace element compositions measured in garnet and monazite, combined with data from thermobarometric calculations and modelling, are used to interpret and develop P-T-t paths.

7.1.1. Garnet trace elements

Garnet is the most voluminous mineral phase to act as a significant HREE and Y reservoir/sink and, therefore, exerts significant control on the bulk rock budget of these elements (Foster et al, 2000, 2002; Gibson et al., 2004; Spear & Pyle, 2002). The distribution of HREEs and Y in garnet can provide insight into its growth and resorption history and its potential impacts on the growth/breakdown of other REE-bearing phases.

Garnet porphyroblasts from the structurally lowest specimen, 502074, show zonation in trace elements. The cores are characterized by high HREE concentrations (e.g. Lu in Fig. 6a) and low Y contents relative to the rims. This is the only specimen analysed that has a negative correlation between HREE and Y. This signature of high HREE and low Y may be attributed to initial growth of garnet cores in a Y-depleted reservoir, which is consistent with the absence of xenotime in this specimen (Corrie & Kohn, 2008; Spear & Pyle, 2002). The rims show a minor increase in HREE but strong relative enrichment in Y and an increase in $(Gd/Yb)_N$ values (Fig. 6a) indicating a breakdown of a HREE- bearing mineral such as monazite, allanite or apatite (Corrie & Kohn, 2008; Spear & Pyle, 2002). Whereas no monazite grains were located in this specimen, abundant apatite inclusions in garnet and partially resorbed allanite near garnet are consistent with the enrichment of Y in garnet rims sourced by the breakdown of those apatite and/or allanite.

Both HREE and Y in garnet from specimen 502071 increase outward from the core, correlated with an increase in negative Eu anomalies towards the rim (Fig. 6b). These increases in HREE and Y are commonly correlated with the prograde growth of garnet during breakdown of HREE- and Y- bearing minerals such as allanite, apatite and/or monazite (Spear & Pyle, 2002). In addition, there is a small but sharp decrease in HREE and Y at the outermost rims, perhaps indicative of synchronous growth of other HREE phases. The occurrence of abundant apatite as both inclusions in garnet and in the matrix, resorbed allanite near garnet grains and the presence of xenotime near the rims of garnet are consistent with both interpretations. Finally, strong negative Eu anomalies increasing away from garnet cores indicate coeval growth with feldspar, consistent with equilibrium modelling results (Fig. 8) that predict an increase in modal proportion of plagioclase along the P-T path.

Garnet from specimens 502068, 502067 and 502050 all show minor zonation in trace element concentrations. Garnet cores, which have almost homogenous profiles for major elements, are characterized by high HREE and Y concentrations that gradually decrease towards the rims (Fig. 6c-e). Whereas, HREE enriched cores with low $(Gd/Yb)_N$ values that gradually change into low HREE and high $(Gd/Yb)_N$ values towards the rims may reflect Rayleigh fractionation of these elements during garnet growth (Otamendi et al., 2002), the sharp increases in HREE and Y at the outermost rims of some of the grains in these specimens (Fig. 6d,e) are interpreted to reflect late-stage sub-solidus dissolution/resorption of garnet and/or breakdown of HREE- bearing minerals across the solidus (Corrie & Kohn, 2008; Soret et al., 2019).

The complex major element zoning observed in garnet from specimen 502056 (Fig. 4f) is also reflected in the trace element concentrations profile (Fig. 6f). Sharp increases in HREE and Y outward from distinct cores are complemented by decreases in negative Eu anomaly and $(Gd/Yb)_N$ values. The relatively lesser negative Eu anomaly and lower $(Gd/Yb)_N$ values observed at the outer core indicate an increase in availability of HREE and Y during crystallization of the garnet outer core and mantle (Fig. 6f). This increase can be explained by garnet growth during breakdown of REE-bearing phases at suprasolidus conditions as calculated by phase equilibrium results. This is further consistent with the breakdown of biotite, plagioclase and/or a REE-rich accessory mineral (e.g. monazite) along the predicted P-T path (Fig. 10). The subsequent outward decrease in HREE and Y towards the rim is interpreted as Rayleigh fractionation during garnet growth (Otamendi et al., 2002). The significant increase in negative Eu anomaly and $(Gd/Yb)_N$ values at the inner rim may indicate coeval garnet growth with REE bearing minerals. This is consistent with the increase in modal proportion of both plagioclase and orthoclase as calculated by phase equilibria modelling (Fig. 10). Further, a distinct but minor enrichment of HREE and Y at the outer rim may indicate re-uptake and resorption at rims during rapid breakdown of feldspar at higher temperature near the solidus, which also is consistent with phase equilibria modelling results.

7.1.2. Monazite trace elements

Similar to garnet, variation in trace element concentrations in monazite can be used to constrain its interaction with other HREE- and Y-bearing mineral phases (Foster et al., 2000; Gibson et al., 2004; Hermann & Rubatto, 2003; Pyle & Spear, 1999; Rubatto et al., 2006, 2013). In medium- to high-grade metamorphic rocks, where garnet and monazite are the primary phases that share the HREE budget, the distribution of HREE and Y in monazite primarily reflects garnet growth and breakdown. For example, monazite grains that grew coevally with garnet, or grew after garnet had already taken up most of the HREE budget, may have relatively low concentrations of HREE and Y, whereas monazite that grew during garnet breakdown, in the absence of garnet or during low garnet modal abundance may have high concentrations of HREE and Y (Foster et al., 2002; 2004; Gibson et al., 2004: Kohn et al., 2005; Pyle & Spear, 1999).

Monazite from 502035 only yielded one Miocene date, impending investigation of temporal trend in chemistry. Monazite from 502073 and 502072 record similar dates and trace element compositions (Figs 11 and 12). Both specimens show two compositionally distinct growth events, one during early to middle Eocene time and another in early to middle Miocene time (Fig. 11). Monazite from the earlier event is characterized by low Y concentrations and low to moderate $(Gd/Yb)_N$ values (Fig. 12), and possibly records earliest prograde metamorphism where monazite grew in the presence of another HREE -bearing phase or grew alone with a small initial reservoir of HREE. Monazite from the younger event show moderate to high Y and low to moderate $(Gd/Yb)_N$ values for both specimens, specimen 502072 shows a weak trend of increasing Y concentration and decreasing $(Gd/Yb)_N$ values with time (Fig. 12). These REE and Y patterns indicate monazite growth during garnet breakdown and/or monazite growth by breakdown of REE phases such as xenotime in the presence of stable garnet. Although no garnet was analyzed for trace elements from these specimens, this interpretation is consistent with the early Miocene garnet Lu-Hf dates obtained from nearby specimen 502074, which is from a similar structural level. The data indicate early Miocene prograde garnet growth followed by minor breakdown of garnet, evident as garnet rims being replaced by late biotite in thin section.

Monazite from specimen 502067 records growth during late Eocene to early Miocene time (Fig. 11). The Y concentrations and $(Gd/Yb)_N$ values measured in monazite do not outline distinct patterns with age (Fig. 12), however, the younger monazite analyses show a decrease in $(Gd/Yb)_N$ values. While the trends of Y concentrations and $(Gd/Yb)_N$ values for older dates are broadly consistent with simultaneous monazite-garnet growth during late Eocene to late Oligocene time, the increase in Y concentrations correlated with decreasing $(Gd/Yb)_N$ values for the younger dates are indicative of garnet breakdown during early Miocene time.

Monazite analyses from specimen 502050 record growth events during early to late Oligocene and late Oligocene to mid-Miocene time (Fig. 11). The early event is associated with low to moderate Y concentrations that increase with younger dates and high to moderate $(Gd/Yb)_N$ values that show the inverse relationship (Fig. 12). Similar trends are also observed in the younger event. These patterns of changing Y concentrations and $(Gd/Yb)_N$ values with time can be interpreted as early monazite growth in the presence of stable garnet and/or breakdown of some HREE-bearing minerals, such as allanite, during Oligocene to early Miocene time, followed by further monazite growth during garnet breakdown in mid-Miocene time.

Monazite from specimen 502056 records two distinct events, one during early to mid-Eocene time and the other spanning late Oligocene to mid-Miocene time (Fig. 11). Monazite with low Y concentrations and low to moderate $(Gd/Yb)_N$ values associated with the early event may record prograde metamorphism, indicating initial monazite growth in presence of another REE-bearing phase or phases. In contrast, monazite with high Y concentrations and low to moderate $(Gd/Yb)_N$ values associated with the late Oligocene to mid-Miocene event indicates monazite recrystallization in the presence of stable or breaking- down garnet, potentially from a REE-buffered reservoir.

7.2. Lu distribution in garnet and garnet ages

Garnet Lu-Hf dates represents a grain-average date, which is influenced by Lu distribution in garnet (Lapen et al., 2003; Smit et al., 2010). In most metapelitic rocks, Lu is strongly partitioned into the cores of garnet grains and therefore Lu-Hf dates are typically interpreted to show some bias towards the growth of said cores (e.g. Kellett et al., 2014; Lapen et al., 2003; Smit et al., 2010; 2014). However, if garnet growth pulses occurred at significantly different times leading to chemically distinct high Lu growth zones, the Lu-Hf analyses may provide mixed dates (Kellett et al., 2014; Kelly et al., 2011; Lapen et al., 2003; Smit et al., 2010). Furthermore, at high temperatures, when garnet resorption or dissolution-regrowth allows re-uptake of Lu back to garnet while Hf is lost to the bulk matrix, it could cause significant 'younging' in Lu-Hf dates (Kelly et al., 2011; Kohn, 2009; Smit et al., 2013)

Garnet in most specimens used for Lu-Hf dating in this study, which record high temperature metamorphism, show normal Rayleigh fractionation of HREE and Lu with a decrease in Lu outwards towards the rim (Fig. 6a-f) and are therefore interpreted to record prograde growth. Both garnet grains analyzed in specimen 502067, however, record significant uptake of Lu (and HREE) at the outermost rims (Fig. 6d). We interpret this increase in Lu at the outermost rim to represent a late- stage dissolution/resorption of garnet across the solidus coeval with breakdown of other HREE- bearing minerals. To account for this late -stage uptake of Lu in specimen 502067, standard Lu budget calculations (e.g. Kellett et al., 2014; Smit et al., 2010) were carried out to investigate the significance of this garnet component and obtain the apparent age for garnet core-rim growth. Based on the average garnet volume, assuming spherical garnet, we estimate that 75 - 80 % of the grain-averaged age is determined by the age of core to inner rim domains, whereas 20 - 25 % of the bulk age represents the outer rim. If we use the monazite age population of ca. 18 Ma, interpreted to reflect final melt crystallization for this specimen, a Lu budget calculation shows garnet core to inner rim growth at ca. 35 Ma (see Table S4 for Lu budget distribution and apparent age calculations). This age is consistent with garnet Lu-Hf ages obtained from subjacent rocks in the Modi Khola region (Table 6), implying that the initial prograde metamorphism in all the rocks structurally above the MCT in Modi Khola region may have been coeval.

7.3. Timing of metamorphism and P-T-t paths

The P-T estimates obtained through phase equilibria modelling and quartz in garnet barometry, coupled with garnet and monazite trace-element compositions, and monazite U-Th-Pb and garnet Lu-Hf age data, provide a powerful multi-component means of constructing P-T-t paths for the specimens analyzed (e.g. Larson et al., 2013; Shrestha et al., 2017, 2019; Weller et al., 2013).

The P-T path obtained from specimen 502074 primarily records prograde metamorphism with minor retrogression (Fig. 7). Although no monazite was located in this specimen, specimens 502073, 502072 and 502035 from the same structural panel yielded dates between ca. 17 and 7 Ma (Fig. 11). The low Y contents in ca. 17 - 13 Ma monazite in those samples (Fig. 12b) are interpreted to indicate coeval growth with garnet during that time. This interpretation is consistent with the garnet Lu-Hf geochronology result from specimen 502074, which records garnet growth ca. 16.8 Ma. The ca. 11 - 7 Ma monazite is characterized by relatively high Y content (Fig. 12b), consistent with garnet breakdown during retrogression (Fig. 14).

The P-T paths for specimen 502071 and 502068, which are from the same structural panel (Fig. 8b, d), show similar initial high-pressure evolutions followed by decompression and cooling. Whereas the inferred P-T path for structurally lower specimen (502071) is completely sub-solidus, the path for the structurally higher specimen (502068) follows a suprasolidus evolution. Predicted anatexis is consistent with petrographic observations of polymineralic and nano-granite-like inclusions observed in garnet from specimen 502068 (Fig. 3e). The absence of monazite in these specimens limits our ability to construct complete P-T-t paths. Still, the garnet Lu-Hf date of ca. 34.0 Ma provides age information on the inferred prograde path of specimen 502071. The Lu-Hf date of ca. 35.1 Ma for specimen 502068 is more difficult to interpret because of its suprasolidus evolution. Because garnet is commonly stable at low P-T, the suprasolidus evolution of 502068 can be interpreted either as a result of it recording only the high-temperature history, an effect of high temperature elemental diffusion moving P-T paths clockwise to high temperature (Spear, 1993), or a combination of both. The homogenous major elemental compositional profile of garnet in specimen 502068 is consistent with high temperature diffusion, so it is possible that the record of initial garnet growth at low metamorphic grades was obliterated. This possibility would be consistent with the interpretation of garnet growth in specimen 502071 from the same structural panel. Monazite dates reported from rocks in other studies from the same structural panel range between ca. 25 - 21 Ma (Corrie & Kohn, 2011). Based on the low

Y contents associated with the monazite analyses, those dates were interpreted to record prograde metamorphism (Corrie & Kohn, 2011). If this interpretation is correct, then prograde metamorphism, which initiated as early as ca. 35 Ma, was still active until ca. 21 Ma. (Fig. 14). With no direct constraint on retrograde metamorphism, it can only be interpreted to post-date ca. 21 Ma.

Specimen 502067 records a decompression and cooling path (Fig. 9b). Monazite from this specimen record protracted growth with moderate to high Y concentrations between ca. 39 and 24 Ma interpreted to reflect simultaneous monazite-garnet growth. This age range overlaps the calculated core-weighted garnet Lu-Hf age of ca. 35 Ma for the growth of garnet core for specimen 502067 and is consistent with initial garnet growth during prograde metamorphism. Similar to specimen 502068, the homogenous major element chemical profiles across garnet in this specimen indicate the effect of thermal diffusion at high temperature, resulting in a loss of the early prograde history. This is consistent with the suprasolidus P-T paths obtained using garnet isopleth thermobarometry that indicate melting during peak metamorphism (Fig. 9b). Although no distinct petrographic evidences of partial melting were observed in this specimen, it could be possible that the textures related to melting were overprinted by late recrystallization textures and/or no significant amount of melt was produced. We, therefore, interpret ca. 39 - 24 Ma to represent protracted garnet growth in subsolidus conditions with ca. 24 Ma constraining the minimum timing for onset of anatexis and peak metamorphism (Fig. 14). The younger monazite growth event, between ca. 23 - 16 Ma, is characterized by monazite domains with high Y concentrations consistent with re-crystallization of monazite during decompression, cooling and garnet breakdown (Kohn et al., 2005; Corrie & Kohn, 2011).

Specimen 502050, from within the same structural panel as specimen 502067, records a similar decompressional cooling P-T path (Fig. 9d). Similar to specimen 502067, monazite from 502050 also records protracted growth. Low- to moderate-Y monazite that yielded ages between ca. 33 and 28 Ma and moderate- to high-Y monazite that yielded ages between ca. 27 - 24 Ma (Fig. 12b) are interpreted to represent simultaneous monazite-garnet growth. The effect of thermal diffusion at high temperature, reflected in a homogenous major element chemical profile in garnet, has resulted in loss of the early prograde history, which is consistent with the suprasolidus P-T paths obtained from phase equilibria modelling. The lack of melt-related petrographic textures in this specimen also indicates either a late stage overprinting by crystallization textures or minimal amount of melt production as discussed above. As such, we interpret ca. 33 - 24 Ma to represent early prograde garnet growth in subsolidus conditions with ca. 24 Ma providing the minimum estimate for timing of melting and peak metamorphism (Fig. 14). Monazite growth between ca. 23 - 15 Ma with high Y concentrations is consistent with post-anatectic re-crystallization of monazite along the retrograde cooling path with garnet breakdown (Corrie & Kohn, 2011; Kohn et al., 2005), thereby providing timing information on the retrograde evolution of this specimen (Fig. 14). Our interpretations for specimen 502067 and 502050 are in agreement with the monazite age interpretation in Corrie and Kohn (2011) for rocks from same structural panel. These authors interpreted ca. 33 - 24 Ma monazite to reflect subsolidus prograde metamorphism and ca. 22 - 17 Ma monazite to have grown during cooling and melt crystallization.

The inferred P-T path for specimen 502056 follows a near-isothermal decompression and cooling (Fig. 10). Similar to structurally underlying specimens, the calculated P-T path shows a suprasolidus evolution. The monazite analysed in this specimen shows two distinct growth events. The older ca. 53 - 40 Ma monazite, which has low Y concentrations, is interpreted to reflect growth during early, low grade metamorphism. This early metamorphism is consistent with the 34.7 Ma Lu-Hf garnet date obtained from the same specimen, which marks the minimum age for garnet growth. The younger growth event, between ca. 24 and 18 Ma, is associated with high Y concentrations, which are consistent with post-anatectic recrystallization of monazite after peak metamorphism during garnet breakdown. A few younger monazite ages ca. 17 - 15 Ma, with intermediate Y concentrations are interpreted to reflect monazite crystallization across the solidus on the retrograde cooling path (Kohn et al., 2005) (Fig. 14). While the P-T paths calculated from phase equilibria modelling show a complete suprasolidus evolution, even for the inferred prograde path, we argue that the initial prograde path likely occurred at sub-solidus conditions followed by further peritectic garnet growth in suprasolidus conditions as discussed above. Garnet major element profiles, which show high-temperature diffusion and reabsorption at the rims, provide further support to this interpretation. Furthermore, the apparent absence of monazite dates between ca. 40 and 24 Ma in this specimen is also consistent with resorption and recrystallization of older monazite in the presence of melt, resulting in the earlier metamorphic history being partially erased at high temperatures (e.g. From et al. 2014; Kohn et al., 2005; Larson et al., 2011). However, monazite dates between ca. 32 - 27 Ma have been reported from rocks at a similar structural level (Corrie & Kohn, 2011). Those dates were interpreted to represent the prograde metamorphic ages (Corrie & Kohn, 2011). If these ages are included in our interpretation, the youngest prograde age of ca. 27 Ma may indicate that melting and eventual cooling of this thrust sheet likely started thereafter (Fig. 14). In addition, the ages between ca. 22 - 17 Ma interpreted as reflecting cooling by Corrie and Kohn (2011) are consistent with our interpretation (Fig. 14).

8. Discussion

8.1. Resolving P-T-t-D discontinuities

Multiple structural discontinuities have been previously identified within the Modi Khola valley (Corrie & Kohn, 2011; Martin et al., 2010, 2015). These include, from structurally lowest to highest, the Main Central thrust, the disputed Bhanuwa fault and the Sinuwa thrust. The thermobarometric and geochronologic results of the present study reveal distinct tectonometamorphic evolutions for the rocks from different structural panels separated by the discontinuities. All specimens structurally above the MCT record a similar late Eocene early prograde history as inferred from garnet Lu-Hf geochronology. However, thermobarometric results and monazite petrochronology from these specimens help provide further information about the thermal regime and juxtaposition of the various rock packages during late prograde to retrograde metamorphism and their subsequent exhumation from the early Oligocene to middle Miocene time.

<u>Specimen 502056 over 502050, 502067 - The Sinuwa thrust</u>

The QuiG barometer returned pressures for all these specimens within analytical uncertainties. Because of a lack of an independent temperature estimate to use with QuiG calculation, P-T estimates obtained from phase equilibria modelling is preferred for tectonic interpretation. P-T estimates from phase equilibria modelling indicates a downward decrease in peak pressure conditions (~ 11 kbar to ~ 8.5 kbar). There is a minor increase in temperature up-structural section with specimen 502056 recording the highest temperature. Moreover, specimen 502050 and 502067 are the only specimens that contain kyanite. This potential break in pressures and presence of K-feldspar *versus* kyanite in the mineral assemblage are consistent with a structural and metamorphic break that juxtaposed rocks across the Sinuwa thrust. In addition, the retrograde metamorphism in the hanging wall was initiated ca. 24 Ma (or as early as ca. 27 Ma) while prograde metamorphism was still ongoing on the footwall until ca. 23 Ma, indicating that movement on the Sinuwa thrust was active during ca. 24 - 23 Ma (Figs 14 and 15).

<u>Specimen 502067 over 502068, 502069, 502071 - The Bhanuwa fault</u>

Both QuiG and phase equilibria modelling show a sharp increase in pressure down structural section (~ 8.5 kbar to ~ 11.3 kbar on phase diagram) at similar temperatures across this structure, indicating a metamorphic break. The variation in mineral assemblage between these rocks, characterized by the absence of kyanite in footwall rocks, is also consistent with the juxtaposition of rock units across the structure. In addition, while retrograde cooling of hanging wall rocks initiated by ca. 23 Ma, the footwall rocks were undergoing prograde metamorphism until ca. 21 Ma (Figs 14 and 15). This diachroneity indicates thrust sense movement across the Bhanuwa fault at ca. 23 - 21 Ma.

<u>Specimen 502071 over 502073, 502074, 502035 - The Main Central Thrust</u>

The sharp difference in pressures between adjacent rocks, ~ 11.4 kbar above compared to ~ 6.6 kbar structurally below the mapped location of the Main Central Thrust, confirms the presence of a tectonometamorphic break. Furthermore, cooling in the hanging wall rocks began sometime after ca. 21 Ma, consistent with the timing of prograde metamorphism of footwall rocks during ca. 17 - 16 Ma (Figs 14 and 15). This synchroneity indicates that thrusting was active during ca. 21 - 16 Ma, driving prograde metamorphism in the footwall of the MCT.

8.2. Tectonic Implications

Metamorphic rocks sampled in the Modi Khola valley record textural, chemical, metamorphic and geochronological evidence that can help characterize the processes active during the early and late stages of the tectonic evolution of the rocks in that region. Our results show that early stage processes are characterized by the progressive juxtaposition of distinct rock packages with unique P-T histories during exhumation. Much of the HMC shows a similar late Eocene prograde metamorphism, implying that initial prograde metamorphism across most of the HMC in the Modi Khola valley was coeval (Figs 14 and 15). Differences, however, are apparent in the timing and P-T conditions at which they experienced both peak and retrograde metamorphism.

The P-T conditions and timing of metamorphism in the rocks across different structures in the Modi Khola valley indicate that the top-to-the north, thrust sense, movement across the ST was active at least during ca. 24 - 23 Ma, which was transferred to the Bhanuwa fault during ca. 23 - 21 Ma. Finally, the thrust sense movement migrated southward, toward the foreland and to the MCT during ca. 21 - 16 Ma (Figs 14 and 15). This down structural section migration of prograde metamorphism, anatexis, cooling and exhumation in the hanging wall resulting in metamorphism in the footwall is consistent with the models of progressive underplating and subsequent duplexing of the HMC in the Himalaya (He et al., 2015; Larson et al., 2015). Corrie and Kohn (2011) preferred their simultaneous cooling Model 2 to explain their results, which shows juxtaposition of already-cooled rocks through out-of-sequence thrusting during transport along a basal thrust. However, our interpretation (Fig. 15) is instead compatible with their Model 1, which shows in-sequence thrusting as the thrust plane progressively migrates down structural section (Corrie & Kohn, 2011) and is further consistent with the prediction of thermomechanical models (e.g. HT111; Jamieson et al., 2006) for the Himalaya (Beaumont et al., 2001; 2004; Jamieson et al., 2004; 2006). The progressive development of a thrust system as identified in this study is compatible with an integrated kinematic model proposed for the Main Central thrust system in West and Central Nepal (Larson et al., 2015), which argues for progressive over-thrusting of the hanging wall followed by under plating and accretion of thrust slices in the footwall, as the overriding thrust sheet is brought towards the foreland (e.g. Carosi et al., 2010; Iaccarino et al., 2015, 2017;

Larson et al., 2013; 2015; Montomoli et al., 2013; 2015; Shrestha et al., 2017; Wang et al., 2016).

Late stage processes recorded in the study area are characterized by the cooling history obtained through published muscovite ^{40}Ar/^{39}Ar ages from Modi Khola valley (Martin et al., 2015). Muscovite from the rocks in the hanging wall of the Sinuwa thrust yielded ^{40}Ar/^{39}Ar ages of 10 Ma, which were interpreted to date the late stage growth of muscovite through hydrothermal alteration (Martin et al., 2015), and are not used here for interpretation of the cooling history. Rocks in the footwall of the Sinuwa thrust/hanging wall of the Banuwa fault, however, yielded muscovite ^{40}Ar/^{39}Ar ages of ca. 18 Ma for larger grains (~ 750 μm) and ca. 16 Ma for smaller grains (~ 200 μm). Muscovite ^{40}Ar/^{39}Ar ages from below the Banuwa fault, only 200 m structurally below the previous specimen, returned muscovite ^{40}Ar/^{39}Ar cooling ages of ca. 13 Ma for larger grains (~ 750 μm) and ca. 10 Ma for smaller grains (~ 200 μm), respectively. In addition, a muscovite cooling age of ca. 7 Ma was obtained from rocks exposed below the MCT. The ^{40}Ar/^{39}Ar obtained from the larger grain fractions from the different structural panels are similar to the final crystallization ages of monazite reported in this study, consistent with rapid cooling during exhumation (Fig. 14). Published apatite fission track data from the same area show rocks on both sides of the Banuwa fault cooled together through ~ 140 ºC at ca. 1 Ma (Nadin & Martin, 2012). Because the muscovite size fractions dated were the same on both sides of the Banuwa fault and they were collected in close proximity, it is unlikely that the differences in ages reflects a significant variation in closure temperature (e.g. Dodson, 1973). As such, the rocks below the Banuwa fault, which cooled ca. 13 - 10 Ma, indicate later cooling and exhumation that those above, which record ca. 18 - 16 Ma cooling ages. As concluded in Martin et al. (2015) this is consistent with cooling of the footwall facilitated by normal-sense reactivation of the Banuwa fault during mid-Miocene time (Martin et al., 2015) (Fig. 15).

This new integrated data set, combined with similar data from other transects along the Himalaya, shows that the assembly of the HMC is principally a result of progressive deformation and juxtaposition of different in-sequence thrust sheets with local out-of-sequence structures (e.g. Ambrose et al., 2015; Larson et al. 2015), followed by late normal-sense reactivation in some locations (Fig. 15). We refer to this as the

Greater Himalayan thrust belt. This progression and sequence of thrusting and faulting is broadly consistent with the predicted geometries (though not absolute ages) from thermo-mechanical models of the Himalaya (Beaumont et al., 2004; Jamieson et al., 2004; 2006) and is generally compatible with thrust and fold belt evolutions observed around the world (e.g. Andes: McQuarrie, 2002; McQuarrie et al., 2005; Western US: Yonkee & Weil; 2010; 2017 and references therein)

9. Conclusions

The results from this study provide new robust constraints on the tectonometamorphic processes that were active within the HMC in the Modi Khola valley during its evolution. The rocks structurally above the MCT all record similar early Eocene prograde metamorphism but differ significantly in P-T conditions and timing of anatexis/peak metamorphism during early Miocene time. Retrograde metamorphism in the hanging walls of the various thrust faults mapped in the area is typically coeval with prograde metamorphism of the rocks in the associated footwall. The detailed P-T-t paths for the various thrust sheets are interpreted to outline in-sequence thrusting during early Miocene time and the development of the Greater Himalayan thrust belt. This was followed by late reactivation of the Bhanuwa fault as a normal-sense structure during mid-Miocene time.

Acknowledgements, Samples, and Data

This study was funded by an NSERC Discovery Grant (RGPIN-2016-06736) and Accelerator Supplement to K. P. Larson, an NSERC Canada Postgraduate Scholarship (PGSD3-489309-2016), University of British Columbia University Graduate Fellowship and Fipke Scholar Grant to S. Shrestha, and an NSERC Discovery Grant (RGPIN-2015-04080) and joint grant from the Canadian Foundation for Innovation and British Columbia Knowledge Development Fund (Nr.:229814) to M.A. Smit. Additional support came from GSA Graduate Student Research Grant and Mitacs Globalink Research Award to S. Shrestha. The authors wish to thank D. Arkinstall and M. Button for their help with the EMP and LA-ICP-MS analysis at the FiLTER facility, UBCO, A. Clark for petrochronology analysis at the LASS Geochronology facility, UCSB and B. Rivera-

Escoto for Raman analysis at the Division of Advanced Materials, IPICYT. Additional figures and tables are provided in supporting information. The processed data used for this study is in the process of being archived and will be available through open science framework (www.osf.io). For review purpose, most of the data are provided in supporting information. There is no conflict of interest with the data and results published in this manuscript.

References

Aleinikoff, J.N., Schenck, W.S., Plank, M.O., Srogi, L., Fanning, C.M., Kamo, S.L., & Bosbyshell, H. (2006). Deciphering igneous and metamorphic events in high-grade rocks of the Wilmington Complex, Delaware: Morphology, cathodoluminescence and backscattered electron zoning, and SHRIMP U-Pb geochronology of zircon and monazite. Geological Society of America Bulletin, 118(1-2), 39-64.

Ambrose, T.K., Larson, K.P., Guilmette, C., Cottle, J.M., Buckingham, H., & Rai, S. (2015). Lateral extrusion, underplating, and out-of-sequence thrusting within the Himalayan metamorphic core, Kanchenjunga, Nepal. Lithosphere, 7(4), 441-464.

Ashley, K.T., Caddick, M.J., Steele-MacInnis, M.J., Bodnar, R.J., & Dragovic, B. (2014a). Geothermobarometric history of subduction recorded by quartz inclusions in garnet. Geochemistry, Geophysics, Geosystems, 15(2), 350-360.

Ashley, K.T., Steele-MacInnis, M., & Caddick, M.J. (2014b). QuIB Calc: A MATLAB® script for geobarometry based on Raman spectroscopy and elastic modeling of quartz inclusions in garnet. Computers and geosciences, 66, 155-157.

Ashley, K.T., Steele-MacInnis, M., Bodnar, R.J., & Darling, R.S. (2016). Quartz-in-garnet inclusion barometry under fire: Reducing uncertainty from model estimates. Geology, 44(9), 699-702.

Beaumont, C., Jamieson, R.A., Nguyen, M.H., & Lee, B. (2001). Himalayan tectonics explained by extrusion of a low-viscosity crustal channel coupled to focused surface denudation. Nature, 414, 738-742.

Beaumont, C., Jamieson, R., Nguyen, M.H., & Medvedev, S. (2004). Crustal channel flows: 1. Numerical models with applications to the tectonics of the Himalayan-Tibetan orogen. Journal of Geophysical Research, 109, B06406.

Blichert-Toft, J. & Albarède, F. (1997). The Lu-Hf isotope geochemistry of chondrites and the evolution of the mantle-crust system. Earth and Planetary Science Letters, 148(1-2), 243-258.

Carosi, R., Montomoli, C., Rubatto, D., Visonà, D., 2010. Late Oligocene high-temperature shear zones in the core of the Higher Himalayan Crystallines (Lower Dolpo, western Nepal). Tectonics 29(4).

Chang, L.L.Y., Howie, R.A., & Zussman, J. (1996). Rock-forming minerals. Non-silicates: Sulphates, carbonates, phosphates and halides. Geological Society of London.

Chernoff, C.B., Carlson, & W.D. (1999). Trace element zoning as a record of chemical disequilibrium during garnet growth. Geology, 27(6), 555-558.

Coggan, R., & Holland, T.J.B. (2002). Mixing properties of phengitic micas and revised garnet-phengite thermometers. Journal of Metamorphic Geology, 20, 683-696.

Corrie, S.L., & Kohn, M.J. (2008). Trace-element distributions in silicates during prograde metamorphic reactions: Implications for monazite formation. Journal of Metamorphic Geology, 26(4), 451-464.

Corrie, S.L., & Kohn, M.J. (2011). Metamorphic history of the central Himalaya, Annapurna region, Nepal, and implications for tectonic models. Geological Society of America Bulletin, 123(9-10), 1863-1879.

Cottle, J.M., Horstwood, M.S.A., & Parrish, R.R. (2009). A new approach to single shot laser ablation analysis and its application to in situ Pb/U geochronology. Journal of Analytical Atomic Spectrometry, 24(10), 1355-1363.

Cottle, J.M., Kylander-Clark, A.R., & Vrijmoed, J.C. (2012). U-Th/Pb geochronology of detrital zircon and monazite by single shot laser ablation inductively coupled plasma mass spectrometry (SS-LA-ICPMS). Chemical Geology, 332, 136-147.

Cottle, J.M., Larson, K.P., & Kellett, D.A. (2015). How does the mid-crust accommodate deformation in large, hot collisional orogens? A review of recent research in the Himalayan orogen. Journal of Structural Geology, 78, 119-133.

Cottle, J.M., Larson, K.P., & Yakymchuk, C. (2018). Contrasting accessory mineral behavior in minimum-temperature melts: Empirical constraints from the Himalayan metamorphic core. Lithos, 312, 57-71.

de Capitani, C., & Brown, T.H. (1987). The computation of chemical equilibrium in complex systems containing non-ideal solutions. Geochimica et Cosmochimica Acta, 51(10), 2639-2652.

de Capitani, C., & Petrakakis, K. (2010). The computation of equilibrium assemblage diagrams with Theriak/Domino software. American Mineralogist, 95(7), 1006-1016.

Dodson, M. (1973). Closure temperature in cooling geochronological and petrological systems. Contributions to Mineralogy and Petrology, 40, pp.259–274.

Enami, M., Nishiyama, T., & Mouri, T. (2007). Laser Raman microspectrometry of metamorphic quartz: A simple method for comparison of metamorphic pressures. American Mineralogist, 92(8-9), 1303-1315.

Foster, G., Kinny, P., Vance, D., Prince, C., & Harris, N. (2000). The significance of monazite U-Th-Pb age data in metamorphic assemblages; a combined study of monazite and garnet chronometry. Earth and Planetary Science Letters, 181(3), 327-340.

Foster, G., Gibson, H.D., Parrish, R., Horstwood, M., Fraser, J., & Tindle, A. (2002). Textural, chemical and isotopic insights into the nature and behaviour of metamorphic monazite. Chemical Geology, 191(1), 183-207.

Foster, G., Parrish, R.R., Horstwood, M.S., Chenery, S., Pyle, J., & Gibson, H.D. (2004). The generation of prograde P-T-t points and paths; a textural, compositional, and chronological study of metamorphic monazite. Earth and Planetary Science Letters, 228(1), 125-142.

From, R., Larson, K., & Cottle, J.M. (2014). Metamorphism and geochronology of the exhumed Himalayan midcrust, Likhu Khola region, east-central Nepal: Recognition of a tectonometamorphic discontinuity. Lithosphere, L381-1.

Frost, B.R., & Chacko, T. (1989). The granulite uncertainty principle: limitations on thermobarometry in granulites. The Journal of Geology, 97(4), 435-450.

Gibson, H.D., Carr, S.D., Brown, R.L., & Hamilton, M.A. (2004). Correlations between chemical and age domains in monazite, and metamorphic reactions involving major pelitic phases: an integration of ID-TIMS and SHRIMP geochronology with Y-Th-U X-ray mapping. Chemical Geology, 211(3), 237-260.

Godet, A., Guilmette, C., Labrousse, L., Smit, M.A., Davis, D.W., Raimondo, T., Vanier, M.A., Charette, B., & Lafrance, I. (2020). Contrasting P-T-t paths reveal a metamorphic discontinuity in the New Quebec Orogen: Insights into Paleoproterozoic orogenic processes. Precambrian Research, 105675.

Godin, L. (2003). Structural evolution of the Tethyan sedimentary sequence in the Annapurna area, central Nepal Himalaya. Journal of Asian Earth Sciences, 22(4), -328.

Grujic, D., Hollister, L.S., & Parrish, R. (2002). Himalayan metamorphic sequence as an orogenic channel: insight from Bhutan. Earth and Planetary Science Letters, 198, 177-191.

Grujic, D., Warren, C.J., & Wooden, J.L. (2011). Rapid synconvergent exhumation of Miocene-aged lower orogenic crust in the eastern Himalaya. Lithosphere, 3, 346-366.

Guilmette, C., Indares, A., & Hébert, R. (2011). High-pressure anatectic paragneisses from the Namche Barwa, Eastern Himalayan Syntaxis: Textural evidence for partial melting, phase equilibria modeling and tectonic implications. Lithos, 124, 66-81.

Guiraud, M., & Powell, R. (2006). P-V-T relationships and mineral equilibria in inclusions in minerals. Earth and Planetary Science Letters, 244(3-4), 683-694.

He, D., Webb, A.A.G., Larson, K.P., Martin, A.J., & Schmitt, A.K. (2015). Extrusion vs. duplexing models of Himalayan mountain building 3: duplexing dominates from the Oligocene to Present. International Geology Review, 1-27.

Henry, D.J., Guidotti, C.V., & Thomson, J.A. (2005). The Ti-saturation surface for low-to-medium pressure metapelitic biotites: Implications for geothermometry and Ti-substitution mechanisms. American Mineralogist, 90(2-3), 316-328.

Hermann, J., & Rubatto, D. (2003). Relating zircon and monazite domains to garnet growth zones: age and duration of granulite facies metamorphism in the Val Malenco lower crust. Journal of Metamorphic Geology, 21(9), 833-852.

Hodges, K.V. (2000). Tectonics of the Himalaya and southern Tibet from two perspectives. Geological Society of America Bulletin, 112(3), 324-350.

Hodges, K.V., Parrish, R.R., & Searle, M.P. (1996). Tectonic evolution of the central Annapurna range, Nepalese Himalayas. Tectonics, 15(6), 1264-1291.

Holland, T.J.B., & Powell, R. (1998). An internally consistent thermodynamic data set for phases of petrological interest. Journal of metamorphic Geology, 16(3), 309-343.

Holland, T.J.B., & Powell, R. (2003). Activity-composition relations for phases in petrological calculations: an asymmetric multicomponent formulation. Contributions to Mineralogy and Petrology, 145(4), 492-501.

Hollister, L.S. (1966). Garnet zoning: an interpretation based on the Rayleigh fractionation model. Science, 154(3757), 1647-1651.

Horstwood, M.S., Foster, G.L., Parrish, R.R., Noble, S.R., & Nowell, G.M. (2003). Common-Pb corrected in situ U-Pb accessory mineral geochronology by LA-MC-ICP-MS. Journal of Analytical Atomic Spectrometry, 18(8), 837-846.

Iaccarino, S., Montomoli, C., Carosi, R., Massonne, H.J., Langone, A., & Visonà, D. (2015). Pressure-temperature-time-deformation path of kyanite-bearing migmatitic paragneiss in the Kali Gandaki valley (Central Nepal): Investigation of Late Eocene-Early Oligocene melting processes. Lithos, 231, 103-121.

Iaccarino, S., Montomoli, C., Carosi, R., Montemagni, C., Massonne, H.J., Langone, A., Jain, A.K., & Visonà, D. (2017). Pressure-Temperature-Deformation-Time

Constraints on the South Tibetan Detachment System in the Garhwal Himalaya (NW India). Tectonics, 36(11), 2281-2304.

Imayama, T., Takeshita, T., Yi, K., Cho, D.-L., Kitajima, K., Tsutsumi, Y., Kayama, M., Nishido, H., Okumura, T., Yagi, K., Itaya, T., & Sano, Y. (2012). Two-stage partial melting and contrasting cooling history within the Higher Himalayan Crystalline Sequence in the far-eastern Nepal Himalaya. Lithos, 134-135, 1-22.

Jamieson, R.A., Beaumont, C., Medvedev, S., & Nguyen, M.H. (2004). Crustal channel flows: 2. Numerical models with implications for metamorphism in the Himalayan-Tibetan orogen. Journal of Geophysical Research: Solid Earth, 109(B6).

Jamieson, R.A., Beaumont, C., Nguyen, M.H., & Grujic, D. (2006). Provenance of the Greater Himalayan Sequence and associated rocks: predictions of channel flow models. Geological Society, London, Special Publications, 268(1), 165-182.

Johnson, T.E., White, R.W., & Powell, R. (2008). Partial melting of metagreywacke: a calculated mineral equilibria study. Journal of Metamorphic Geology, 26(8), 837-853.

Kellett, D.A., Cottle, J.M., & Smit, M. (2014). Eocene deep crust at Ama Drime, Tibet: Early evolution of the Himalayan orogen. Lithosphere, L350-1.

Kelly, E.D., Carlson, W.D., & Connelly, J.N. (2011). Implications of garnet resorption for the Lu-Hf garnet geochronometer: an example from the contact aureole of the Makhavinekh Lake Pluton, Labrador. Journal of Metamorphic Geology, 29(8), 901-916.

Kohn, M.J. (2009). Models of garnet differential geochronology. Geochimica et Cosmochimica Acta, 73(1), 170-182.

Kohn, M.J. (2014a). Himalayan metamorphism and its tectonic implications. Annual Review of Earth and Planetary Sciences, 42, 381-419.

Kohn, M.J. (2014b). "Thermoba-Raman-try": Calibration of spectroscopic barometers and thermometers for mineral inclusions. Earth and Planetary Science Letters, 388, 187-196.

Kohn, M.J., & Spear, F. (2000). Retrograde net transfer reaction insurance for pressure-temperature estimates. Geology, 28(12), 1127-1130.

Kohn, M.J., Wieland, M.S., Parkinson, C.D., & Upreti, B.N. (2005). Five generations of monazite in Langtang gneisses: implications for chronology of the Himalayan metamorphic core. Journal of Metamorphic Geology, 23(5), 399-406.

Konrad-Schmolke, M., O'Brien, P.J., de Capitani, C. & Carswell, D.A. (2008). Garnet growth at high-and ultra-high pressure conditions and the effect of element fractionation on mineral modes and composition. Lithos, 103(3-4), pp.309-332.

Kylander-Clark, A.R., Hacker, B.R., & Cottle, J.M. (2013). Laser-ablation split-stream ICP petrochronology. Chemical Geology, 345, 99-112.

Lapen, T.J., Johnson, C.M., Baumgartner, L.P., Mahlen, N.J., Beard, B.L., & Amato, J.M. (2003). Burial rates during prograde metamorphism of an ultra-high-pressure terrane: an example from Lago di Cignana, western Alps, Italy. Earth and Planetary Science Letters, 215(1), 57-72.

Larson, K.P. (2018). Refining the structural framework of the Khimti Khola region, east-central Nepal Himalaya, using quartz textures and c-axis fabrics. Journal of Structural Geology, 107, 142-152.

Larson, K.P., & Cottle, J.M. (2014). Midcrustal Discontinuities and the Assembly of the Himalayan mid-crust. Tectonics, 33(5), 718-740.

Larson, K.P., Ali, A., Shrestha, S., Soret, M., Cottle, J.M., & Ahmad, R. (2018). Timing of metamorphism and deformation in the Swat valley, northern Pakistan: Insight into garnet-monazite HREE partitioning. Geoscience Frontiers, 10(3), 849-861.

Larson, K.P., Ambrose, T.K., Webb, A.G., Cottle, J.M., & Shrestha, S. (2015). Reconciling Himalayan midcrustal discontinuities: the Main Central thrust system. Earth and Planetary Science Letters, 429, 139-146.

Larson, K.P., Cottle, J.M., & Godin, L. (2011). Petrochronologic record of metamorphism and melting in the upper Greater Himalayan sequence, Manaslu-Himal Chuli Himalaya, west-central Nepal. Lithosphere, 3(6), 379-392.

Larson, K.P., Gervais, F., & Kellett, D. (2013). A P-T-t-D discontinuity in east-central Nepal: implications for the evolution of the Himalayan mid-crust. Lithos, 179, 275-292.

Larson, K.P., Kellett, D.A., Cottle, J.M., King, J., Lederer, G., & Rai, S.M. (2016). Anatexis, cooling, and kinematics during orogenesis: Miocene development of the Himalayan metamorphic core, east-central Nepal. Geosphere, 12(5), 1575-1593.

Le Fort, P. (1975). Himalayas: the collided range. Present knowledge of the continental arc. American Journal of Science, 275(1), 44.

Long, S.P., & McQuarrie, N. (2010). Placing limits on channel flow: Insights from the Bhutan Himalaya. Earth and Planetary Science Letters, 290, 375-390.

Ludwig, K.R. (2003). Isoplot 3.00: A geochronological toolkit for Microsoft Excel. Berkeley Geochronology Center Special Publication, 4, 70.

Mahar, E.M., Baker, J.M., Powell, R., Holland, T.J.B., & Howell, N. (1997). The effect of Mn on mineral stability in metapelites. Journal of Metamorphic Geology, 15(2), 223-238.

Martin, A.J. (2009). Sub-millimeter heterogeneity of yttrium and chromium during growth of semi-pelitic garnet. Journal of Petrology, 50(9), 1713-1727.

Martin, A.J. (2017). A review of Himalayan stratigraphy, magmatism, and structure. Gondwana Research, 49, 42-80.

Martin, A.J., Burgy, K.D., Kaufman, A.J., & Gehrels, G.E. (2011). Stratigraphic and tectonic implications of field and isotopic constraints on depositional ages of Proterozoic Lesser Himalayan rocks in central Nepal. Precambrian Research, 185(1-2), 1-17.

Martin, A. J., Copeland, P., & Benowitz, J. A. (2015). Muscovite $^{40}Ar/^{39}Ar$ ages help reveal the Neogene tectonic evolution of the southern Annapurna Range, central Nepal. Geological Society, London, Special Publications, 412, SP412-5.

Martin, A.J., DeCelles, P.G., Gehrels, G.E., Patchett, P.J., & Isachsen, C. (2005). Isotopic and structural constraints on the location of the Main Central thrust in the Annapurna Range, central Nepal Himalaya. Geological Society of America Bulletin, 117(7-8), 926-944.

Martin, A.J., Ganguly, J., & DeCelles, P.G. (2010). Metamorphism of Greater and Lesser Himalayan rockskohn exposed in the Modi Khola valley, central Nepal. Contributions to Mineralogy and Petrology, 159, 203-223.

McDonough, W.F., & Sun, S.S. (1995). The composition of the Earth. Chemical geology, 120(3), 223-253.

McKinney, S.T., Cottle, J.M., & Lederer, G.W. (2015). Evaluating rare earth element (REE) mineralization mechanisms in Proterozoic gneiss, Music Valley, California. GSA Bulletin, 127(7-8), 1135-1152.

McQuarrie, N. (2002). The kinematic history of the central Andean fold-thrust belt, Bolivia: Implications for building a high plateau. Geological Society of America Bulletin, 114(8), 950-963.

McQuarrie, N., Horton, B.K., Zandt, G., Beck, S. & DeCelles, P.G. (2005). Lithospheric evolution of the Andean fold–thrust belt, Bolivia, and the origin of the central Andean plateau. Tectonophysics, 399(1-4), 15-37.

Montomoli, C., Carosi, R., & Iaccarino, S. (2015). Tectonometamorphic discontinuities in the Greater Himalayan Sequence: a local or a regional feature? In: Mukherjee, S., Carosi, R., van der Beek, P., Mukherjee, B.K., Robinson, D.M. (Eds.), Tectonics of the Himalaya. Geological Society, London, Special Publications, 412(1), 25-41.

Montomoli, C., Iaccarino, S., Carosi, R., Langone, A., & Visona, D. (2013). Tectonometamorphic discontinuities within the Greater Himalayan Sequence in Western Nepal (Central Himalaya): Insights on the exhumation of crystalline rocks. Tectonophysics, 608, 1349-1370.

Mukherjee, S., Koyi, H.A., & Talbot, C.J. (2012). Implications of channel flow analogue models for extrusion of the Higher Himalayan Shear Zone with special reference to the out-of sequence thrusting. International Journal of Earth Sciences, 101, 253-272.

Nadin, E.S., & Martin, A.J. (2012). Apatite thermochronometry within a knickzone near the Higher Himalaya front, central Nepal: No resolvable fault motion in the past one million years. Tectonics, 31(2).

Otamendi, J.E., Jesús, D., Douce, A.E.P., & Castro, A. (2002). Rayleigh fractionation of heavy rare earths and yttrium during metamorphic garnet growth. Geology, 30(2), 159-162.

Palin, R.M., Weller, O.M., Waters, D.J., & Dyck, B. (2016). Quantifying geological uncertainty in metamorphic phase equilibria modelling; a Monte Carlo assessment and implications for tectonic interpretations. Geoscience Frontiers, 7(4), 591-607.

Pattison, D.R., & Bégin, N.J. (1994). Zoning patterns in orthopyroxene and garnet in granulites: implications for geothermometry. Journal of Metamorphic Geology, 12(4), 387-410.

Pearce, N.J., Perkins, W.T., Westgate, J.A., Gorton, M.P., Jackson, S.E., Neal, C.R., & Chenery, S.P. (1997). A compilation of new and published major and trace element data for NIST SRM 610 and NIST SRM 612 glass reference materials. Geostandards newsletter, 21(1), 115-144.

Pyle, J.M., & Spear, F.S. (1999). Yttrium zoning in garnet: coupling of major and accessory phases during metamorphic reactions. Geological Materials Research, 1(6), 1-49.

Pyle, J.M., & Spear, F.S., (2003). Four generations of accessory-phase growth in low-pressure migmatites from SW New Hampshire. American Mineralogist, 88(2-3), 338-351.

Raimondo, T., Payne, J., Wade, B., Lanari, P., Clark, C., & Hand, M. (2017). Trace element mapping by LA-ICP-MS: assessing geochemical mobility in garnet. Contributions to Mineralogy and Petrology, 172(4), 17.

Regis, D., Warren, C.J., Young, D., & Roberts, N.M. (2014). Tectono-metamorphic evolution of the Jomolhari massif: Variations in timing of syn-collisional metamorphism across western Bhutan. Lithos, 190, 449-466.

Rubatto, D., Chakraborty, & S., Dasgupta, S. (2013). Timescales of crustal melting in the Higher Himalayan Crystallines (Sikkim, Eastern Himalaya) inferred from trace element-constrained monazite and zircon chronology. Contributions to Mineralogy and Petrology, 165(2), 349-372.

Rubatto, D., Hermann, J., & Buick, I.S. (2006). Temperature and bulk composition control on the growth of monazite and zircon during low-pressure anatexis (Mount Stafford, central Australia). Journal of Petrology, 47(10), 1973-1996.

Schärer, U. (1984). The effect of initial230Th disequilibrium on young UPb ages: the Makalu case, Himalaya. Earth and Planetary Science Letters, 67(2), 191-204.

Scherer, E.E., Münker, C., & Mezger, K. (2001). Calibration of the lutetium-hafnium clock. Science, 293(5530), 683-687.

Schmidt, C., & Ziemann, M.A. (2000). In-situ Raman spectroscopy of quartz: A pressure sensor for hydrothermal diamond-anvil cell experiments at elevated temperatures. American Mineralogist, 85(11-12), 1725-1734.

Searle, M.P., Law, R.D., Godin, L., Larson, K.P., Streule, M.J., Cottle, J.M., & Jessup, M.J. (2008). Defining the Himalayan Main Central Thrust in Nepal. Journal of the Geological Society, London, 165, 523-534.

Shrestha, S., Larson, K. P., Duesterhoeft, E., Soret, M., & Cottle, J.M. (2019). Thermodynamic modelling of phosphate minerals and its implications for the development of P-T-t histories: A case study in garnet - monazite bearing metapelites. Lithos, 334 - 335, 141 - 160.

Shrestha, S., Larson, K.P., Guilmette, C., & Smit, M.A. (2017). The P-T-t evolution of the exhumed Himalayan metamorphic core in the Likhu Khola region, East Central Nepal. Journal of Metamorphic Geology, 35(6), 663-693.

Smit, M.A., Hacker, B.R., & Lee, J. (2014). Tibetan garnet records early Eocene initiation of thickening in the Himalaya. Geology 42(7), 591-594.

Smit, M.A., Scherer, E.E., Bröcker, M., & van Roermund, H.L. (2010). Timing of eclogite facies metamorphism in the southernmost Scandinavian Caledonides by Lu-Hf and Sm-Nd geochronology. Contributions to Mineralogy and Petrology, 159(4), 521-539.

Smit, M.A., Scherer E.E., & Mezger, K. (2013). Lu-Hf and Sm-Nd garnet geochronology: Chronometric closure and implications for dating petrological processes. Earth and Planetary Science, 381, 222-233.

Söderlund, U., Patchett, P.J., Vervoort, J.D., & Isachsen, C.E. (2004). The ^{176}Lu decay constant determined by Lu-Hf and U-Pb isotope systematics of Precambrian mafic intrusions. Earth and Planetary Science Letters, 219(3-4), 11-324.

Soret, M., Larson, K.P., Cottle, J.M., Smit, M., Johnson, A., Shrestha, S., Ali, & A., Faisal, S. (2019). Mesozoic to Cenozoic tectono-metamorphic history of the South Pamir - Hindu Kush (Chitral, NW Pakistan): insights from phase equilibria modelling, and garnet - monazite petrochronology. Journal of Metamorphic Geology, 37(5), 633-666.

Spear, F.S. (1993). Metamorphic phase equilibria and pressure-temperature-time paths (Vol. 1). Washington, DC: Mineralogical Society of America.

Spear, F.S., & Pyle, J.M. (2002). Apatite, monazite, and xenotime in metamorphic rocks. Reviews in Mineralogy and Geochemistry, 48(1), 293-335.

Tinkham, D.K., Zuluaga, C.A., & Stowell, H.H. (2001). Metapelite phase equilibria modeling in MnNCKFMASH: The effect of variable Al_2O_3 and MgO/(MgO+ FeO) on mineral stability. American Mineralogist, 88(7), 1174-1174.

Tracy, R.J., Robinson, P., & Thompson, A.B. (1976). Garnet composition and zoning in the determination of temperature and pressure of metamorphism, central Massachusetts. American Mineralogist, 61(7-8), 762-775.

Vielzeuf, D., Baronnet, A., Perchuk, A.L., Laporte, D., & Baker, M.B. (2007). Calcium diffusivity in alumino-silicate garnets: an experimental and ATEM study. Contributions to Mineralogy and Petrology, 154(2), 153-170.

Wang, J.M., Zhang, J.J., & Wang, X.X (2013). Structural kinematics, metamorphic P-T profiles and zircon geochronology across the Greater Himalayan Crystalline Complex in south-central Tibet: implication for a revised channel flow. Journal of Metamorphic Geology, 31, 607-628.

Wang, J.M., Zhang, J.J., Liu, K., Zhang, B., Wang, X.X., Rai, S., & Scheltens, M. (2016). Spatial and temporal evolution of tectonometamorphic discontinuities in the central Himalaya: Constraints from P-T paths and geochronology. Tectonophysics, 679, 41-60.

Weller, O.M., St-Onge, M.R., Waters, D.J., Rayner, N., Searle, M.P., Chung, S.L., Palin, R.M., Lee, Y.H., & Xu, X. (2013). Quantifying Barrovian metamorphism in the

Danba Structural Culmination of eastern Tibet. Journal of Metamorphic Geology, 31(9), 909-935.

White, R.W., & Powell, R. (2002). Melt loss and the preservation of granulite facies mineral assemblages. Journal of Metamorphic Geology, 20(7), 621-632.

White, R.W., Pomroy, N.E., & Powell, R. (2005). An in situ metatexite-diatexite transition in upper amphibolite facies rocks from Broken Hill, Australia. Journal of Metamorphic Geology, 23(7), 579-602.

White, R.W., Powell, R., Holland, T.J.B., & Worley, B.A. (2000). The effect of TiO_2 and Fe_2O_3 on metapelitic assemblages at greenschist and amphibolite facies conditions: mineral equilibria calculations in the system K_2O-FeO-MgO-Al_2O_3-SiO_2-H_2O-TiO_2-Fe_2O_3. Journal of Metamorphic Geology, 18(5), 497-512.

White, R.W., Powell, R., & Holland, T.J.B. (2007). Progress relating to calculation of partial melting equilibria for metapelites. Journal of Metamorphic Geology, 25(5), 511-527.

Whitney, D.L., & Evans, B.W. (2010). Abbreviations for names of rock-forming minerals. American mineralogist, 95(1), 185.

Woodsworth, G.J. (1977). Homogenization of zoned garnets from pelitic schists. Canadian Mineralogist, 15, 230-242.

Yakymchuk, C., & Godin, L. (2012). Coupled role of deformation and metamorphism in the construction of inverted metamorphic sequences: an example from far-northwest Nepal. Journal of Metamorphic Geology, 30, 315-353.

Yin, A., & Harrison, T.M. (2000). Geologic evolution of the Himalayan-Tibetan orogen. Annual Review of Earth and Planetary Sciences, 28(1), 211-280.

Yonkee, A. & Weil, A.B. (2010). Reconstructing the kinematic evolution of curved mountain belts: Internal strain patterns in the Wyoming salient, Sevier thrust belt, USA. Bulletin, 122(1-2), 24-49.

Yonkee, A. & Weil, A.B. (2017). Structural evolution of an en echelon fold system within the Laramide foreland, central Wyoming: From early layer-parallel shortening to fault propagation and fold linkage. Lithosphere, 9(5), 828-850.

Figure 1. Geological and metamorphic zonation map of the Modi Khola area. (a) Simplified geologic map of the Nepalese Himalaya (after He et al., 2015; Larson et al., 2015). Study area for this project is outlined by the white box. (b) Geological and metamorphic zonation map of the Modi Khola transect outlining the sample locations and inferred discontinuities (based on Corrie & Kohn, 2011; Martin et al., 2005; 2010).

Figure 2. QEMSCAN maps showing the general textures of selected thin sections. The legend shows respective colour codes assigned to individual mineral groups. White zones are holes through which thin section glass was analyzed.

Figure 3. Photomicrographs of microstructures observed in thin sections (PPL - Plane Polarized Light; XPL - Cross Polarized Light). (a) Sigmoidal inclusion trails in garnet connected to main foliation. (b) Muscovite and biotite forming lepidoblastic schistosity wrapping around garnet porphyroblasts, quartz and plagioclase in strain shadow. (c) Late chlorite and biotite locally replacing garnet at the rims. (d) Preferentially oriented biotite and muscovite forming schistosity. (e) Muscovite and biotite in the strain caps, quartz and plagioclase in the strain shadows, lobate inclusions of quartz in garnet. (f) Biotite and aligned kyanite defining schistosity, kyanite growing on an early biotite. (g) Biotite anastomosing around a garnet porphyroblast, kyanite occurs as both aligned blades and inclusions in garnet. (h) Oriented biotite and muscovite forming schistosity, garnet primarily associated with mica. (i) Embayed kyanite being replaced by quartz and biotite. (j) Garnet porphyroblast with lobate quartz inclusions, biotite replacing garnet at rims. (k) Large garnet porphyroblast with quartz inclusions, biotite replacing garnet at rims. (l) Plagioclase in contact with K-feldspar showing myrmekite texture.

Figure 4. Major element compositional profiles of selected garnet. Primary y-axis shows proportion of X(Prp), X(Grs) and X(Sps), whereas secondary y-axis shows proportion of X(Alm). Core (C), Mantle (M), Inner Rim (IR) and Outer rim (OR).

Figure 5. Major element compositions of biotite. Plots of Ti (a.p.f.u) vs Mg# [Mg/(Fe^{2+}+Mg] are shown.

Figure 6. Trace element compositional profiles of selected garnet. Profiles show Lu and Y concentration (ppm) with 1-sigma error bars on primary axis, whereas secondary axis shows $(Gd/Yb)_N$ ratio and Eu anomaly $(Eu/Eu^*)_N$.

Figure 7. Phase equilibria modelling results for specimen 502074. (a) Phase diagram calculated using XRF whole-rock composition. The phase diagram is calculated with water in excess. The observed peak assemblage is highlighted with bold letters. Black stippled box shows location of intersection of measured mineral proportion (± 1 % modal envelope) for major minerals (see Fig. S3). (b) Phase diagram overlain by the interpreted P-T path based on the intersection of compositional isopleths of major silicate minerals. The isopleths of Grt_Mg# (brown), Grt_Grs (light blue) and Bt_Mg# (green) are shown. The letters with circles indicate the locations of compositions taken along the garnet profile: Core (C), Mantle (M), Rim (R) and Outer rim (R with stippled circle). The polygons outline the intersections of isopleths from similar domains in all analyzed garnet grains (see Figs 4 and S1 for details).

Figure 8. Phase equilibria modelling results for specimens 502071 and 502068. (a, c) Phase diagrams calculated using XRF whole-rock composition. Each phase diagram shows a subsolidus region modelled with excess water (left) and a suprasolidus region modelled with a saturated solidus (right). The observed peak assemblage is highlighted with bold letters. Black stippled box shows location of intersection of measured mineral proportion (± 1 % modal envelope) for major minerals (see Fig. S3). (b, d) Phase diagrams overlain by the interpreted P-T path based on the intersection of compositional isopleths of major silicate minerals. The isopleths of Grt_Mg# (brown), Grt_Grs (light blue) and Pl_An (dark blue) are shown. The letters with circles indicate the locations of compositions taken along the garnet profile: Core (C), Mantle (M), Rim (R) and Outer rim (R with stippled circle). The polygons outline the intersections of isopleths from similar domains in all analyzed garnet grains (see Figs 4 and S1 for details). Also overlain is pressure calculated with QuIG barometry.

Figure 9. Phase equilibria modelling results for specimens 502067 and 502050. (a, c) Phase diagrams calculated using XRF whole-rock composition. Each phase diagram shows a subsolidus region modelled with excess water (left) and a suprasolidus region modelled with a saturated solidus (right). The observed peak assemblage is highlighted with bold letters. Black stippled box shows location of intersection of measured mineral proportion (± 1 % modal envelope) for major minerals (see Fig. S3). (b, d) Phase diagrams overlain by the interpreted P-T path based on the intersection of compositional isopleths of major silicate minerals. The isopleths of Grt_Mg# (brown), Grt_Grs (light blue) and Pl_An (dark blue) are shown. The letters with circles indicate the locations of compositions taken along the garnet profile: Core (C), Mantle (M), Rim (R) and Outer rim (R with stippled circle). The polygons outline the intersections of isopleths from similar domains in all analyzed garnet grains (see Figs 4 and S1 for details). Also overlain is pressure calculated with QuIG barometry.

Figure 10. Phase equilibria modelling results for specimen 502056. (a) Phase diagram calculated using XRF whole-rock composition. Phase diagram shows a subsolidus region modelled with excess water (left) and a suprasolidus region modelled with a saturated solidus (right). The observed peak assemblage is highlighted with bold letters. Black stippled box shows location of intersection of measured mineral proportion (± 1 % modal envelope) for major minerals (see Fig. S3). (b) Phase diagram overlain by the interpreted P-T path based on the intersection of compositional isopleths of major silicate minerals. The isopleths of Grt_Mg# (brown), Grt_Grs (light blue) and Pl_An (dark blue) are shown. The letters with circles indicate the locations of compositions taken along the garnet profile: Core (C), Mantle (M), Rim (R) and Outer rim (R with stippled circle). The polygons outline the intersections of isopleths from similar domains in all analyzed garnet grains (see Figs 4 and S1 for details). Also overlain is pressure calculated with QuIG barometry.

Figure 11. Geochronology data. (a - f) U-Th-Pb concordia plots illustrating ranges of spot dates obtained from in-situ monazite analyses, with 2-sigma ellipses coloured to indicate measured Y concentration for each spot. Warmer colours indicate higher

concentrations. Only dates < 60 Ma shown. Inset shows probability plots of dates for each specimen.

Figure 12. Monazite age probability plot and trace element data. (a) Probability plots of dates obtained from all the specimens. The dark brown color shows the probability plot for all samples combined. (b) Y vs date plot. (c) $(Gd/Yb)_N$ ratio vs date plot. (d) Europium anomaly $(Eu/Eu^*)_N$ vs date plot.

Figure 13. Garnet Lu-Hf isochrons for selected specimens. MSWD = mean square of weighted deviates, n = number of aliquots.

Figure 14. Interpreted P-T-t paths for the rocks from Modi Khola region.

Figure 15. Schematic kinematic model of the evolution of the rock packages in the study area based on the results presented herein and previously published constraints (Larson et al., 2015, 2016; Martin et al., 2015).

Tables

Table 1. Petrographic description of selected specimens.

Table 2. Observed mineral assemblages.

Table 3. XRF Bulk composition (wt. %) used for phase equilibria modelling.

Table 4. Bulk compositions in cation moles used as input for phase equilibria modelling.

Table 5. Raman data and calculated QuiG pressures.

Table 6. Garnet Lu-Hf isotope and age data.

Figure.

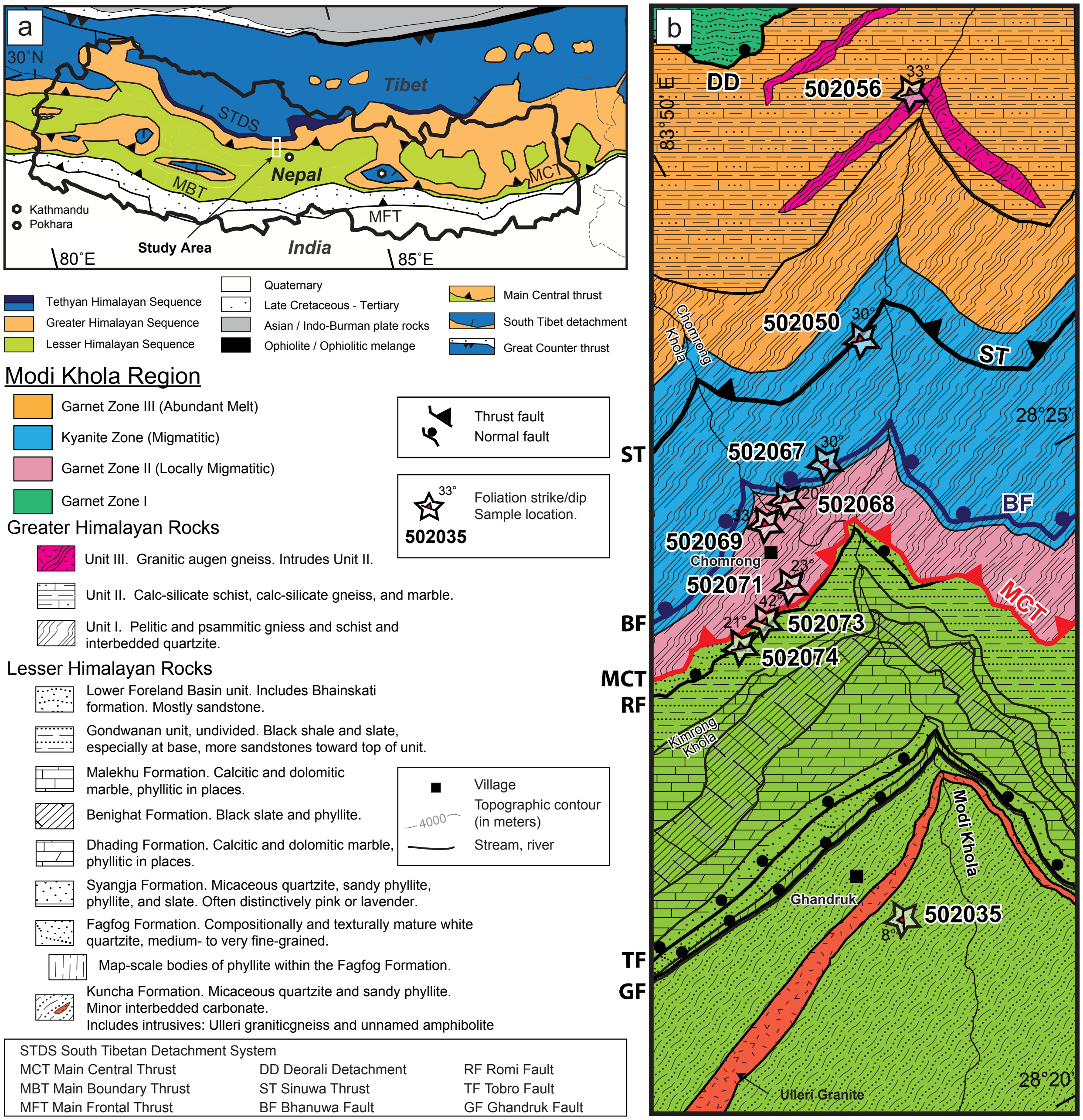

Fig. 1. Geological and metamorphic zonation map of the Modi Khola area. (a) Simplified geologic map of the Nepalese Himalaya (after He et al., 2015; Larson et al., 2015). Study area for this project is outlined by the white box. (b) Geological and metamorphic zonation map of the Modi Khola transect outlining the sample locations and inferred discontinuities (based on Corrie & Kohn, 2011; Martin et al., 2005, 2010).

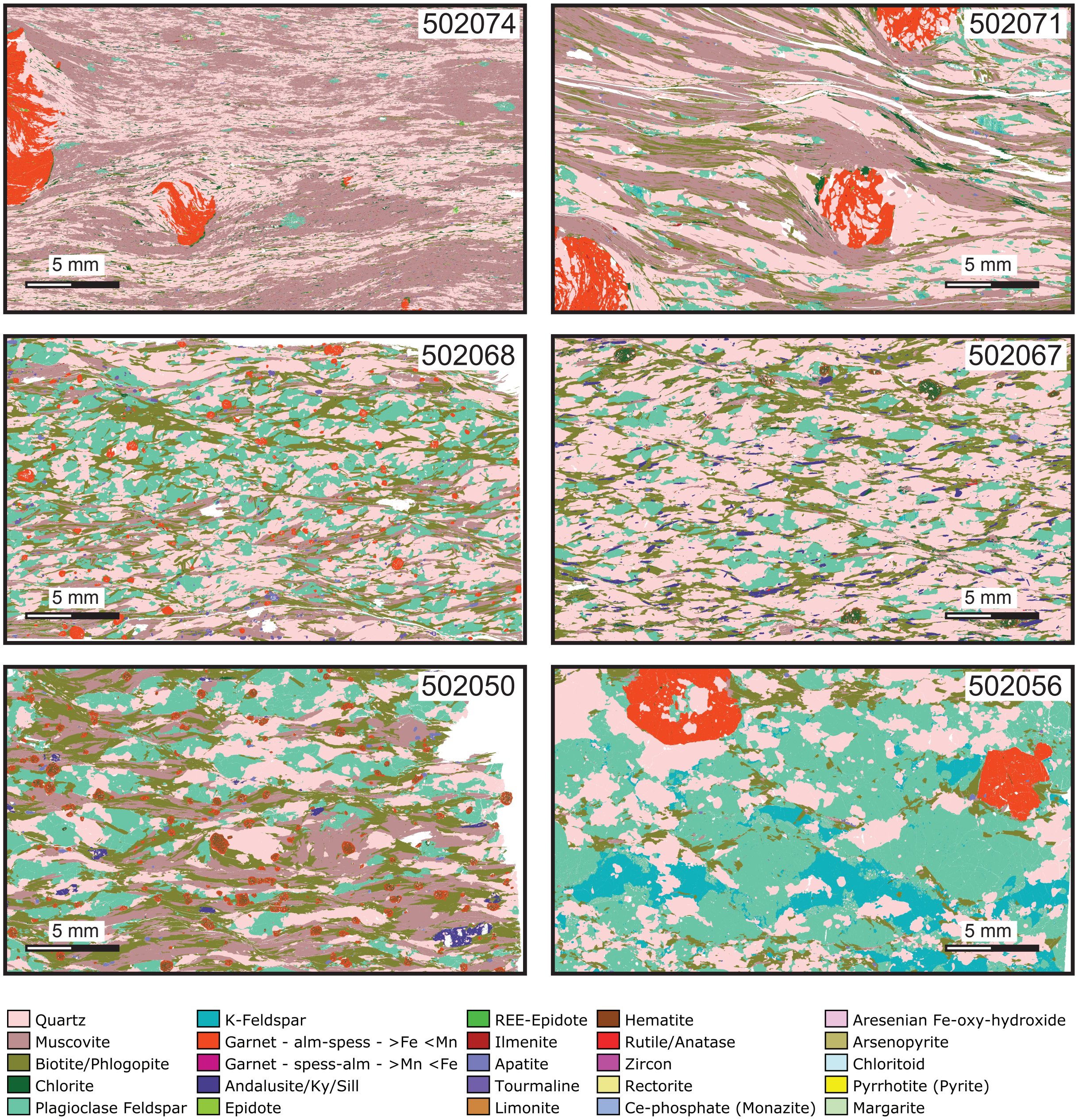

Fig. 2. QEMSCAN maps showing the general textures of selected thin sections. The legend shows respective colour codes assigned to individual mineral groups. White zones are holes through which thin section glass was analyzed.

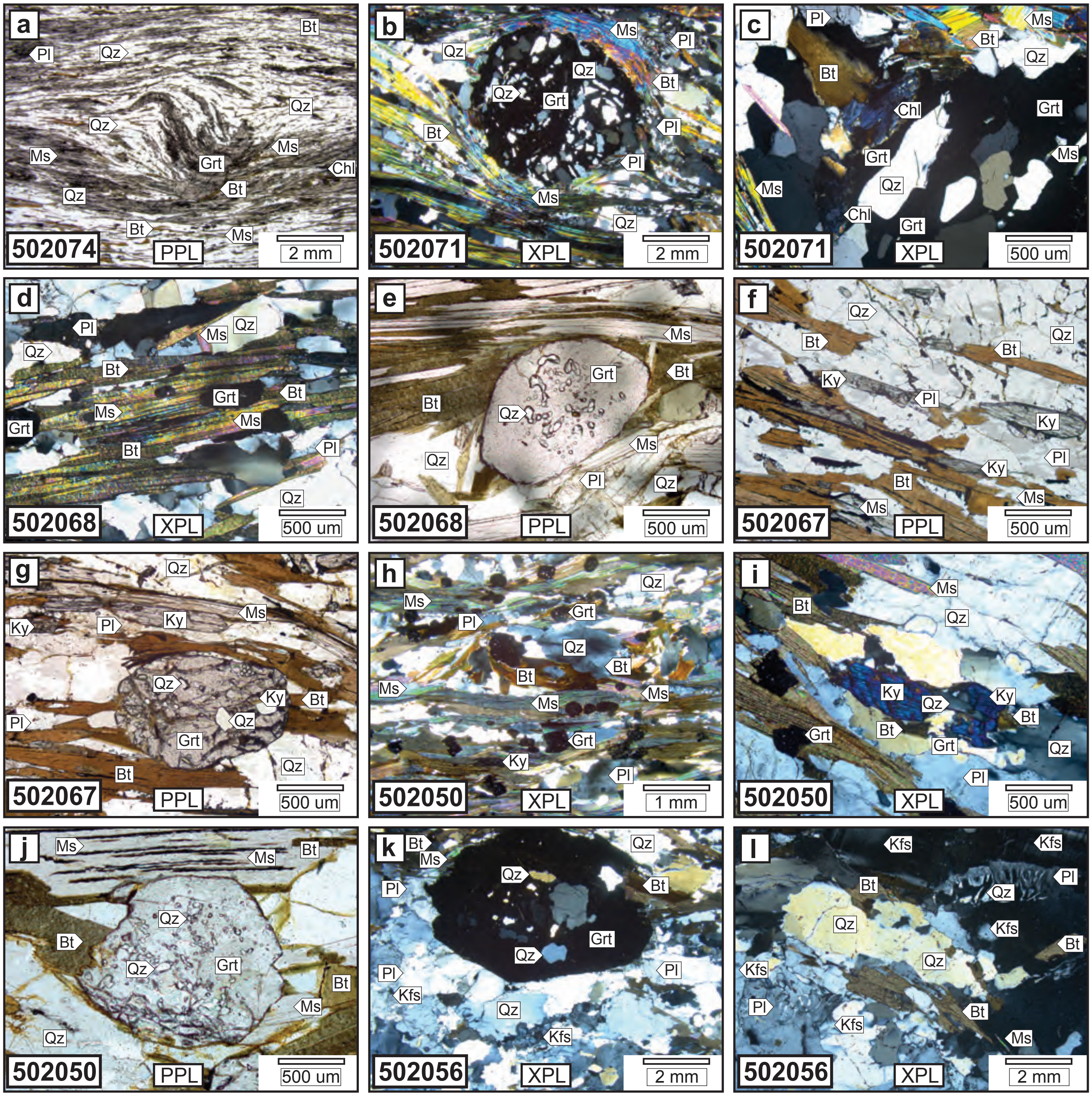

Fig. 3. Photomicrographs of microstructures observed in thin sections (PPL - Plane Polarized Light; XPL - Cross Polarized Light). (a) Sigmoidal inclusion trails in garnet connected to main foliation. (b) Muscovite and biotite forming lepidoblastic schistosity wrapping around garnet porphyroblasts, quartz and plagioclase in strain shadow. (c) Late chlorite and biotite locally replacing garnet at the rims. (d) Preferentially oriented biotite and muscovite forming schistosity. (e) Muscovite and biotite in the strain caps, quartz and plagioclase in the strain shadows, lobate inclusions of quartz in garnet. (f) Biotite and aligned kyanite defining schistosity, kyanite growing on an early biotite. (g) Biotite anastomosing around a garnet porphyroblast, kyanite occurs as both aligned blades and inclusions in garnet. (h) Oriented biotite and muscovite forming schistosity, garnet primarily associated with mica. (i) Embayed kyanite being replaced by quartz and biotite. (j) Garnet porphyroblast with lobate quartz inclusions, biotite replacing garnet at rims. (k) Large garnet porphyroblast with quartz inclusions, biotite replacing garnet at rims. (l) Plagioclase in contact with K-feldspar showing myrmekite texture.

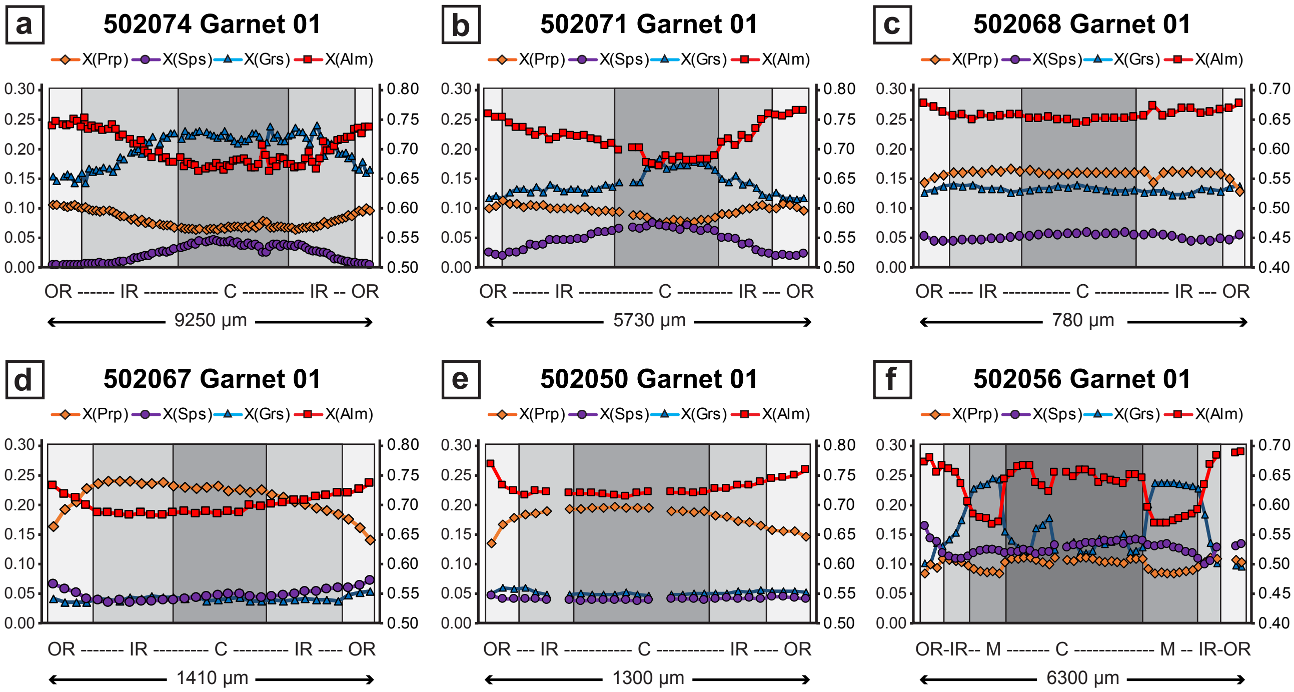

Fig. 4. Major element compositional profiles of selected garnet. Primary y-axis shows proportion of X(Prp), X(Grs) and X(Sps), whereas secondary y-axis shows proportion of X(Alm). Core (C), Mantle (M), Inner Rim (IR) and Outer rim (OR).

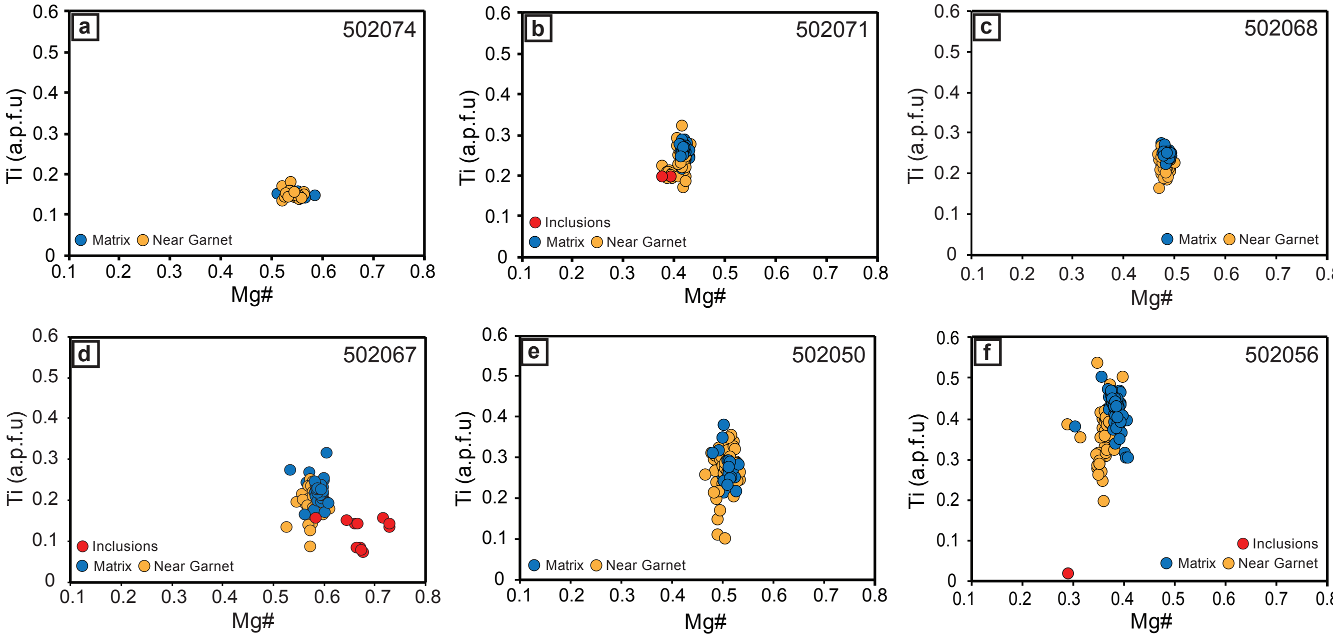

Fig. 5. Major element compositions of biotite. Plots of Ti (a.p.f.u) vs Mg# [Mg/(Fe2++Mg] are shown.

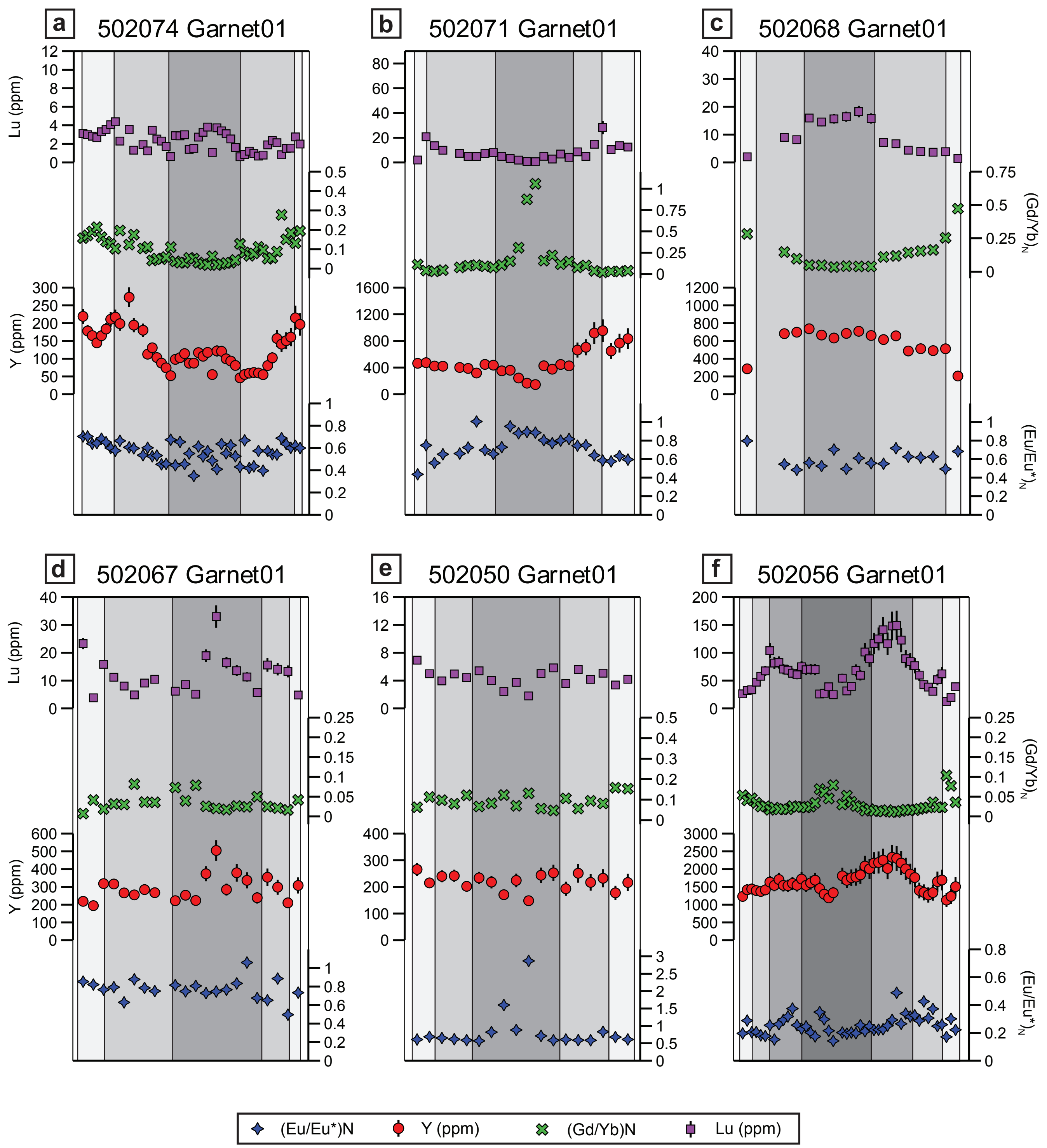

Fig. 6. Trace element compositional profiles of selected garnet. Profiles show Lu and Y concentration (ppm) with 1-sigma error bars on primary axis, whereas secondary axis shows (Gd/Yb)N ratio and Eu anomaly (Eu/Eu*)N.

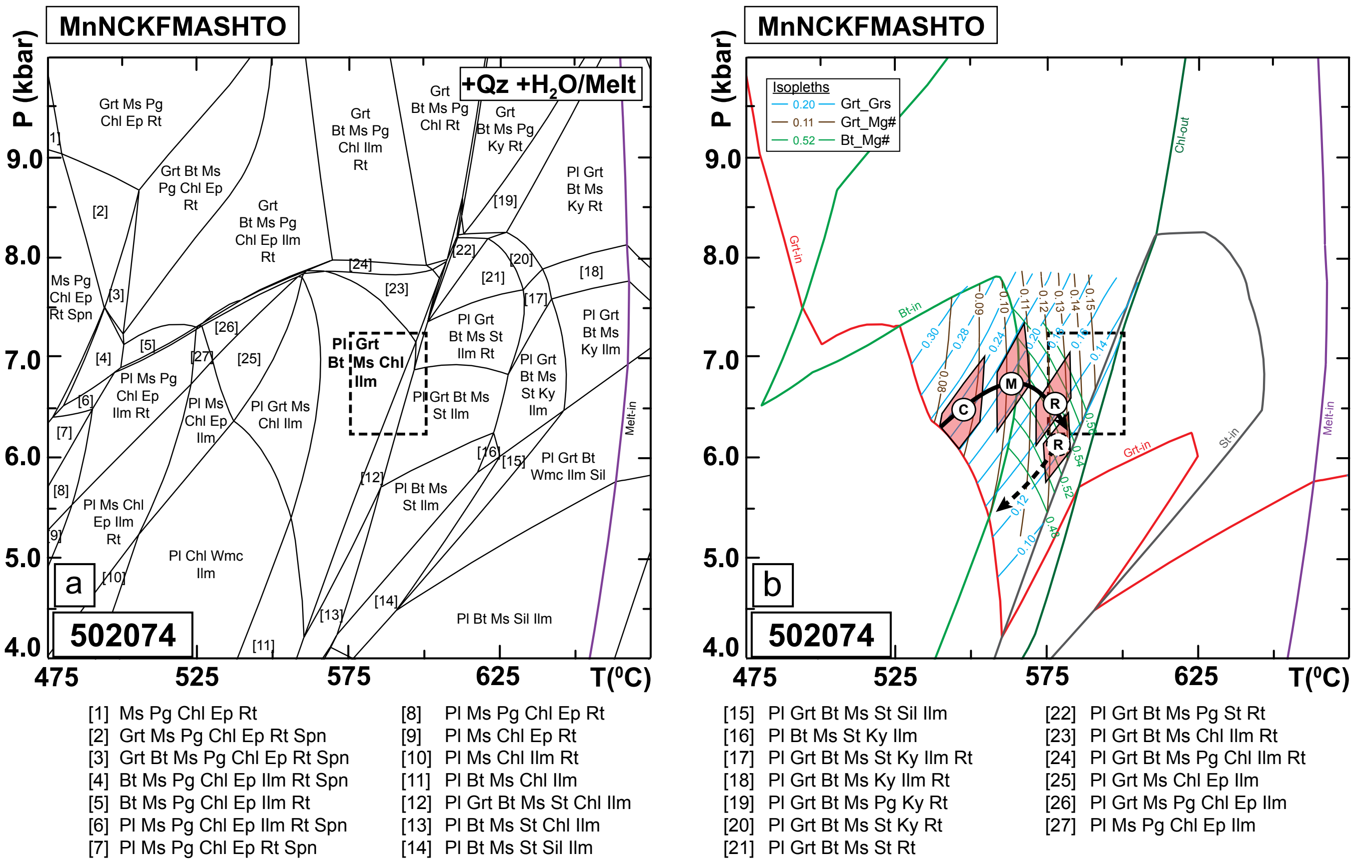

Fig. 7. Phase equilibria modelling results for specimen 502074. (a) Phase diagram calculated using XRF whole-rock composition. The phase diagram is calculated with water in excess. The observed peak assemblage is highlighted with bold letters. Black stippled box shows location of intersection of measured mineral proportion (± 1 % modal envelope) for major minerals (see Fig. S3). (b) Phase diagram overlain by the interpreted P-T path based on the intersection of compositional isopleths of major silicate minerals. The isopleths of Grt_Mg# (brown), Grt_Grs (light blue) and Bt_Mg# (green) are shown. The letters with circles indicate the locations of compositions taken along the garnet profile: Core (C), Mantle (M), Rim (R) and Outer rim (R with stippled circle). The polygons outline the intersections of isopleths from similar domains in all analyzed garnet grains (see Figs 4 and S1 for details).

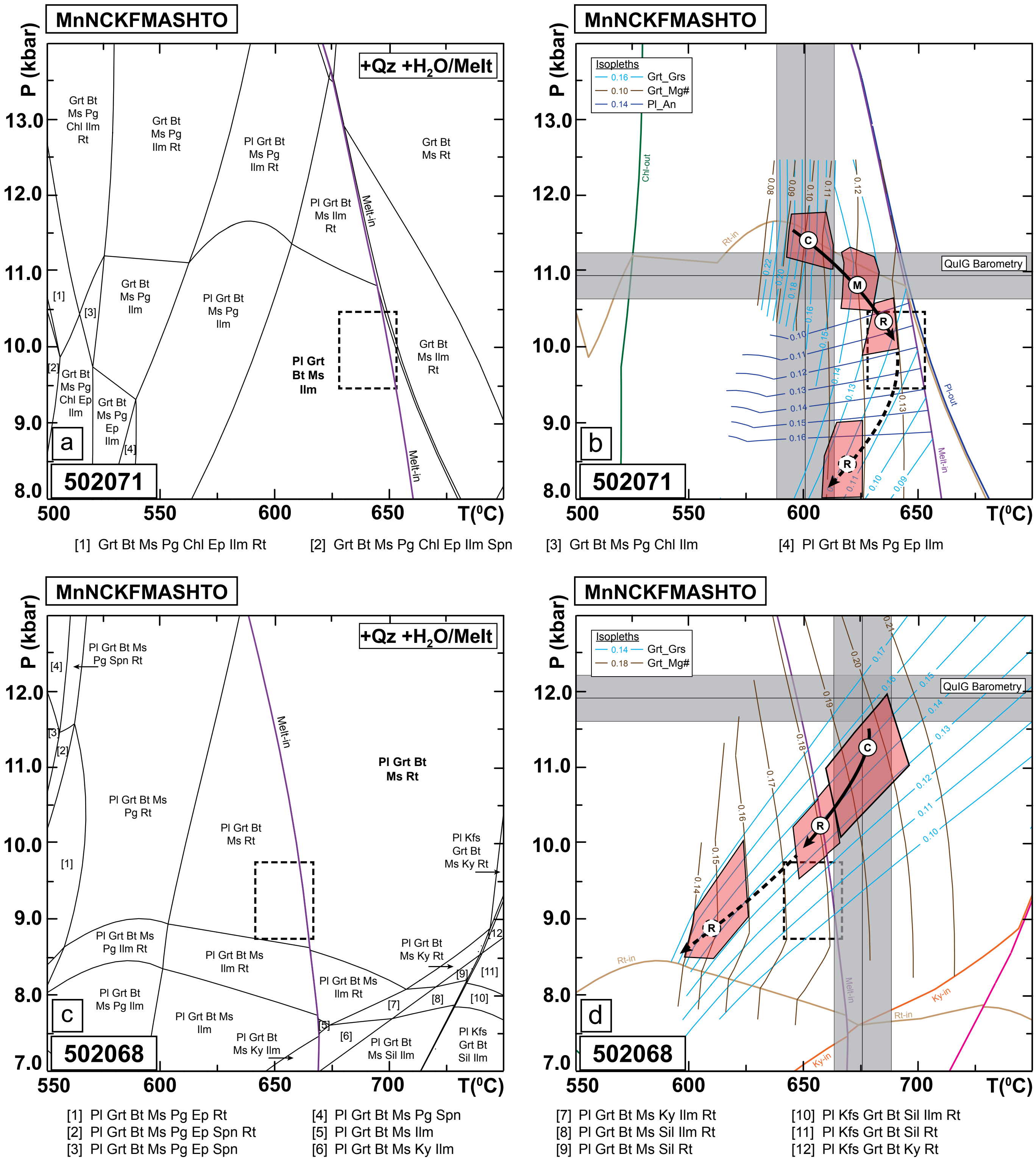

Fig. 8. Phase equilibria modelling results for specimens 502071 and 502068. (a, c) Phase diagrams calculated using XRF whole-rock composition. Each phase diagram shows a subsolidus region modelled with excess water (left) and a suprasolidus region modelled with a saturated solidus (right). The observed peak assemblage is highlighted with bold letters. Black stippled box shows location of intersection of measured mineral proportion (± 1 % modal envelope) for major minerals (see Fig. S3). (b, d) Phase diagrams overlain by the interpreted P-T path based on the intersection of compositional isopleths of major silicate minerals. The isopleths of Grt_Mg# (brown), Grt_Grs (light blue) and Pl_An (dark blue) are shown. The letters with circles indicate the locations of compositions taken along the garnet profile: Core (C), Mantle (M), Rim (R) and Outer rim (R with stippled circle). The polygons outline the intersections of isopleths from similar domains in all analyzed garnet grains . Also overlain is pressure calculated with QuIG barometry.

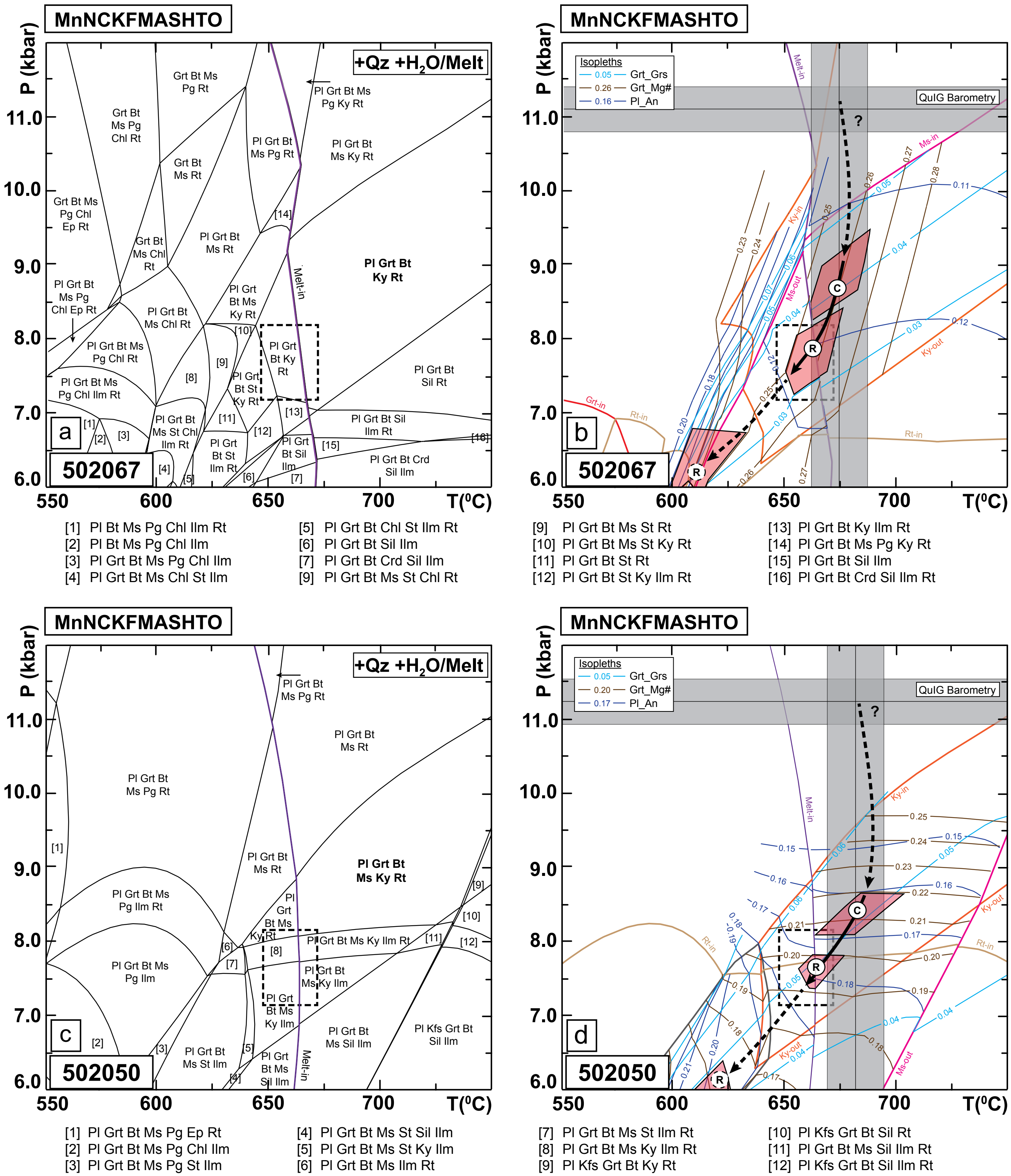

Fig. 9. Phase equilibria modelling results for specimens 502067 and 502050. (a, c) Each phase diagram shows a subsolidus region modelled with excess water (left) and a suprasolidus region modelled with a saturated solidus (right). The observed peak assemblage is highlighted with bold letters. Black stippled box shows location of intersection of measured mineral proportion (± 1 % modal envelope) for major minerals. (b, d) Phase diagrams overlain by the interpreted P-T path based on the intersection of compositional isopleths of major silicate minerals. The letters with circles indicate the locations of compositions taken along the garnet profile: Core (C), Mantle (M), Rim (R) and Outer rim (R with stippled circle). Also overlain is pressure calculated with QuIG barometry.

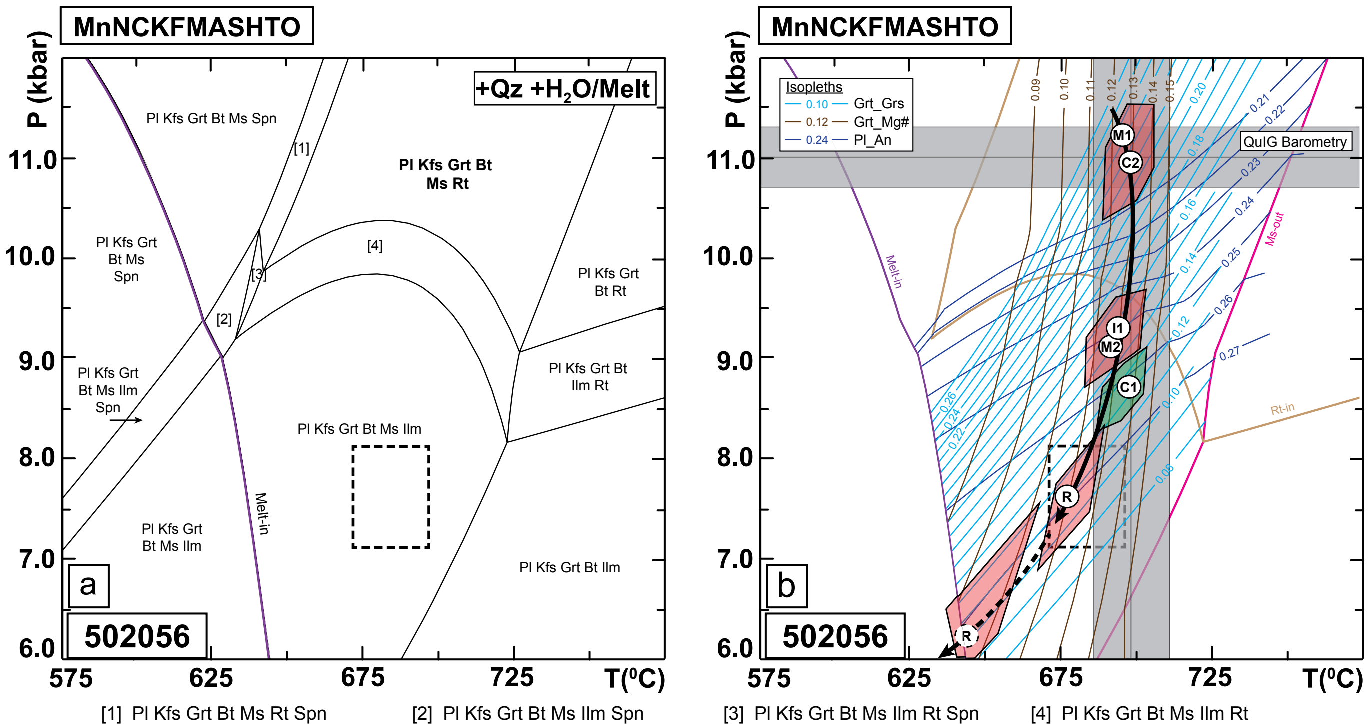

Fig. 10. Phase equilibria modelling results for specimen 502056. (a) Phase diagram calculated using XRF whole-rock composition. Phase diagram shows a subsolidus region modelled with excess water (left) and a suprasolidus region modelled with a saturated solidus (right). The observed peak assemblage is highlighted with bold letters. Black stippled box shows location of intersection of measured mineral proportion (± 1 % modal envelope) for major minerals (see Fig. S3). (b) Phase diagram overlain by the interpreted P-T path based on the intersection of compositional isopleths of major silicate minerals. The isopleths of Grt_Mg# (brown), Grt_Grs (light blue) and Pl_An (dark blue) are shown. The letters with circles indicate the locations of compositions taken along the garnet profile: Core (C), Mantle (M), Rim (R) and Outer rim (R with stippled circle). The polygons outline the intersections of isopleths from similar domains in all analyzed garnet grains (see Figs 4 and S1 for details). Also overlain is pressure calculated with QuIG barometry.

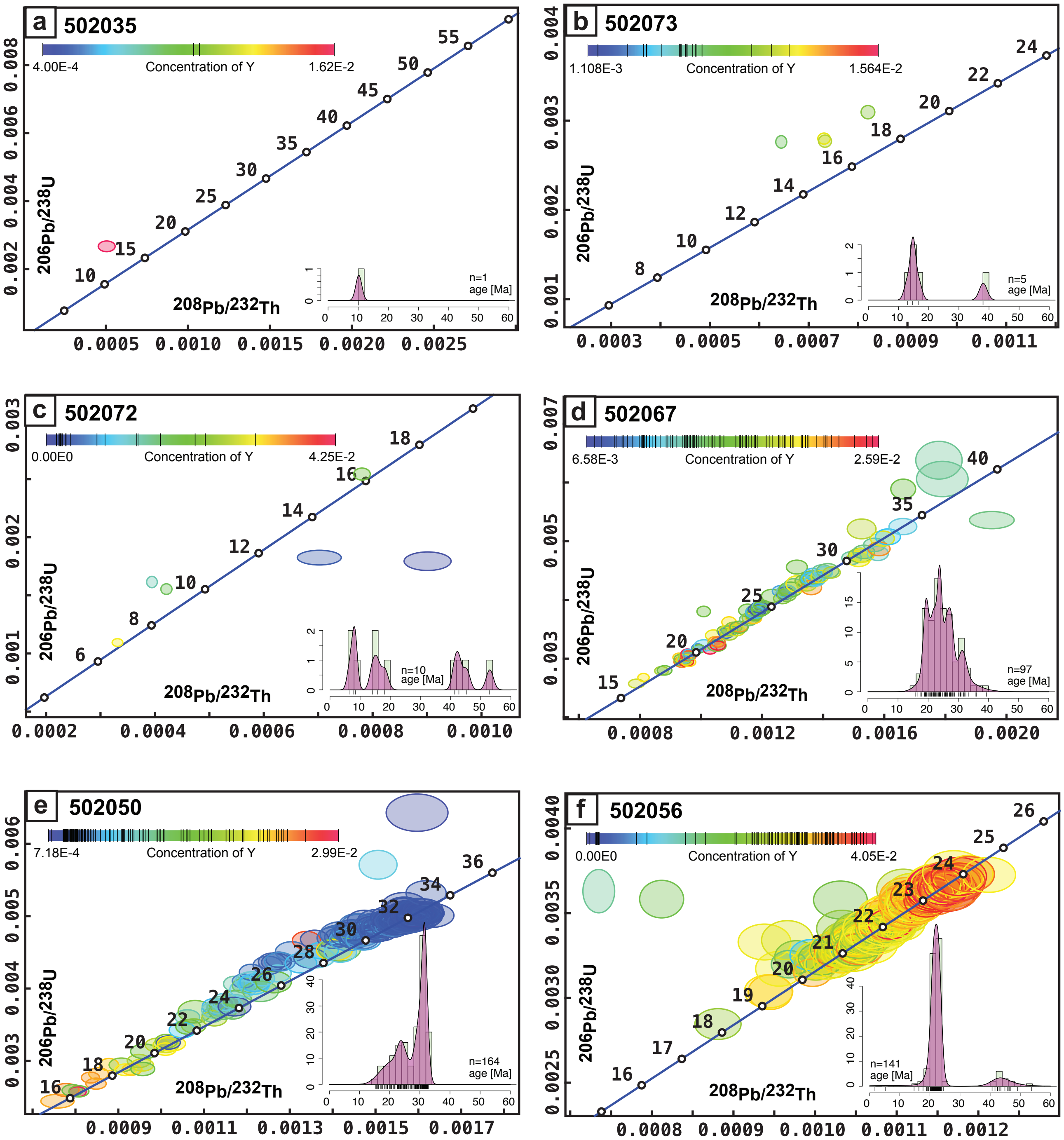

Fig. 11. Geochronology data. (a - f) U-Th-Pb concordia plots illustrating ranges of spot dates obtained from in-situ monazite analyses, with 2-sigma ellipses coloured to indicate measured Y concentration for each spot. Warmer colours indicate higher concentrations. Only dates < 60 Ma shown. Inset shows probability plots of dates for each specimen.

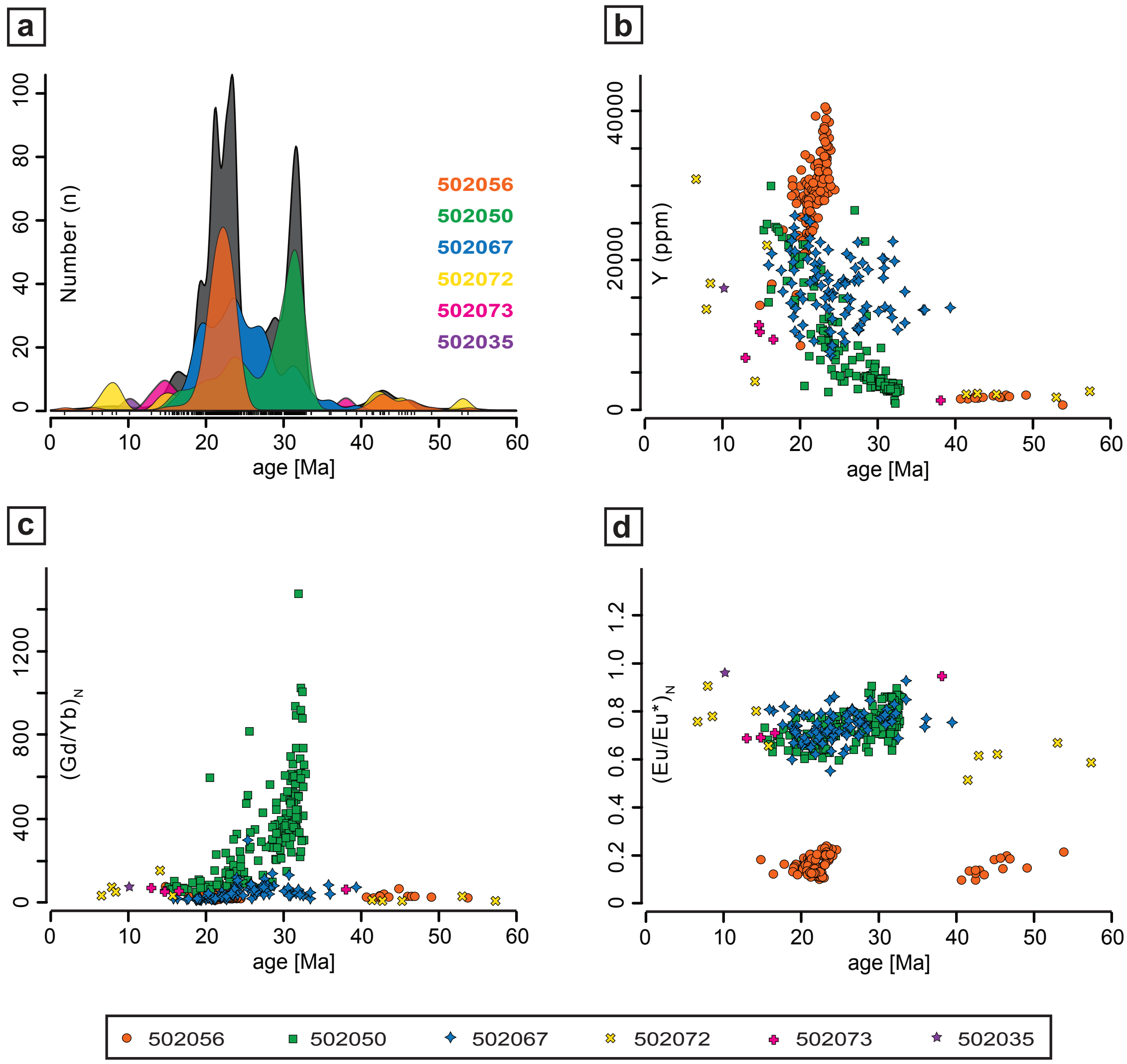

Fig. 12. Monazite age probability plot and trace element data. (a) Probability plots of dates obtained from all the specimens. The dark brown color shows the probability plot for all samples combined. (b) Y vs date plot. (c) (Gd/Yb)N ratio vs date plot. (d) Europium anomaly (Eu/Eu*)N vs date plot.

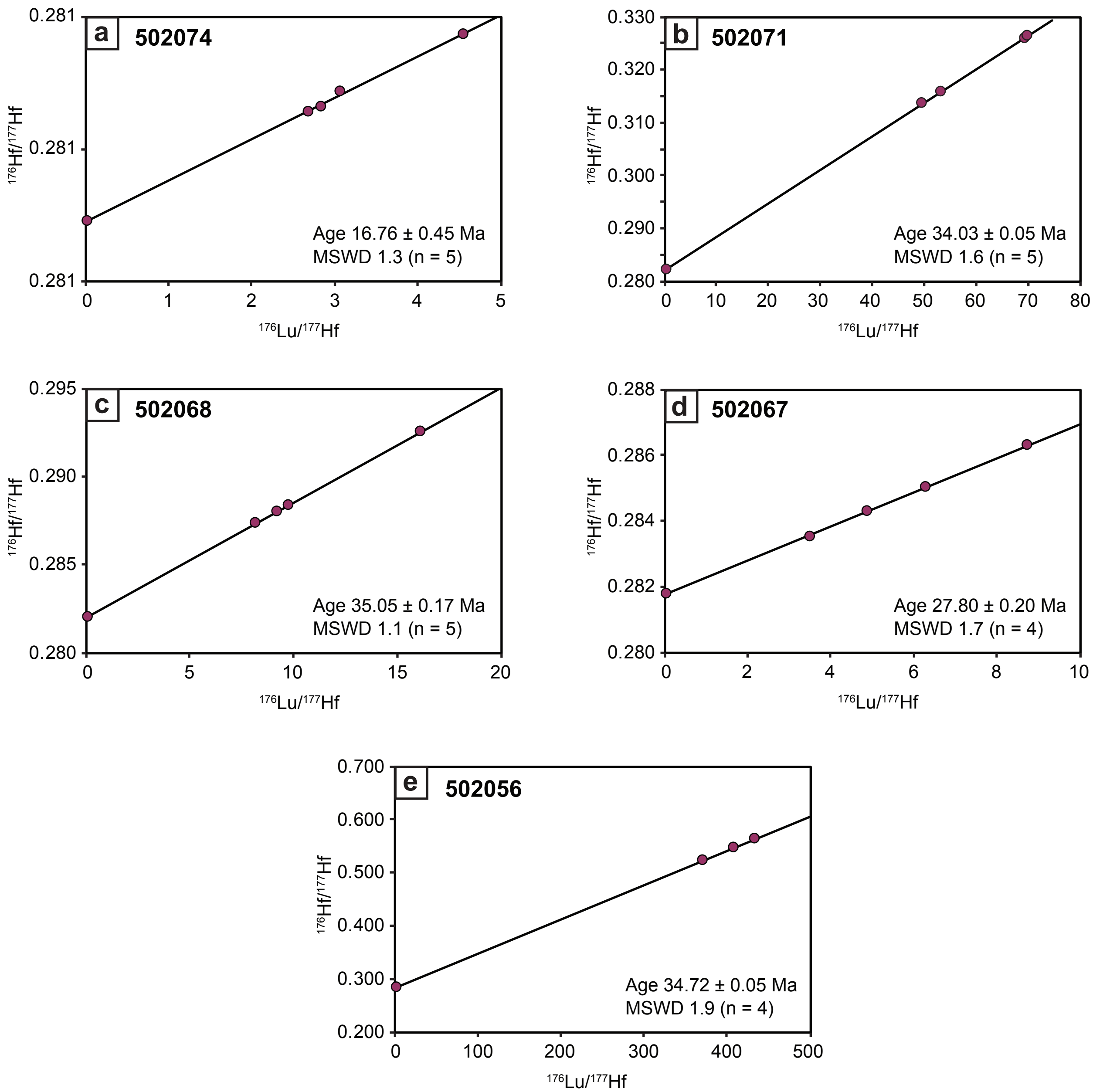

Fig. 13. Garnet Lu-Hf isochrons for selected specimens. MSWD = mean square of weighted deviates, n = number of aliquots.

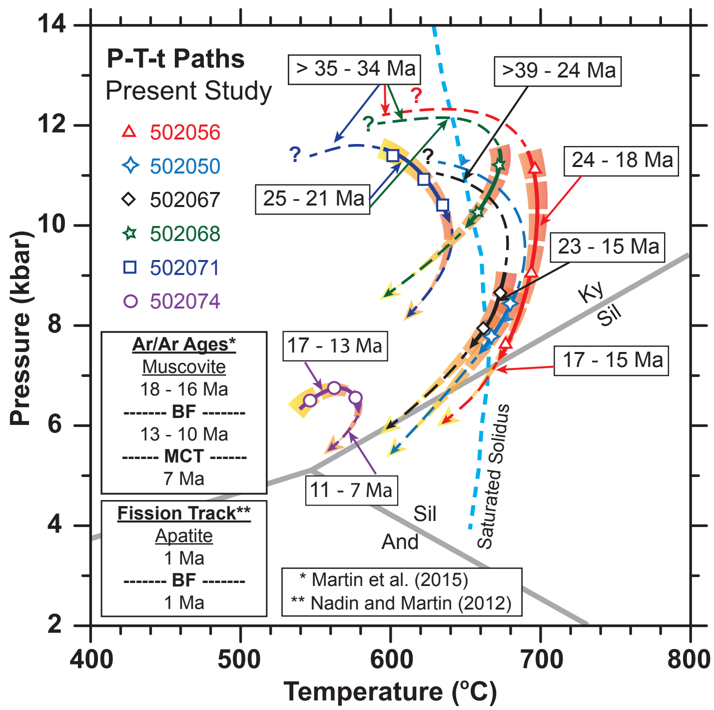

Fig. 14. Interpreted P-T-t paths for the rocks from Modi Khola region.

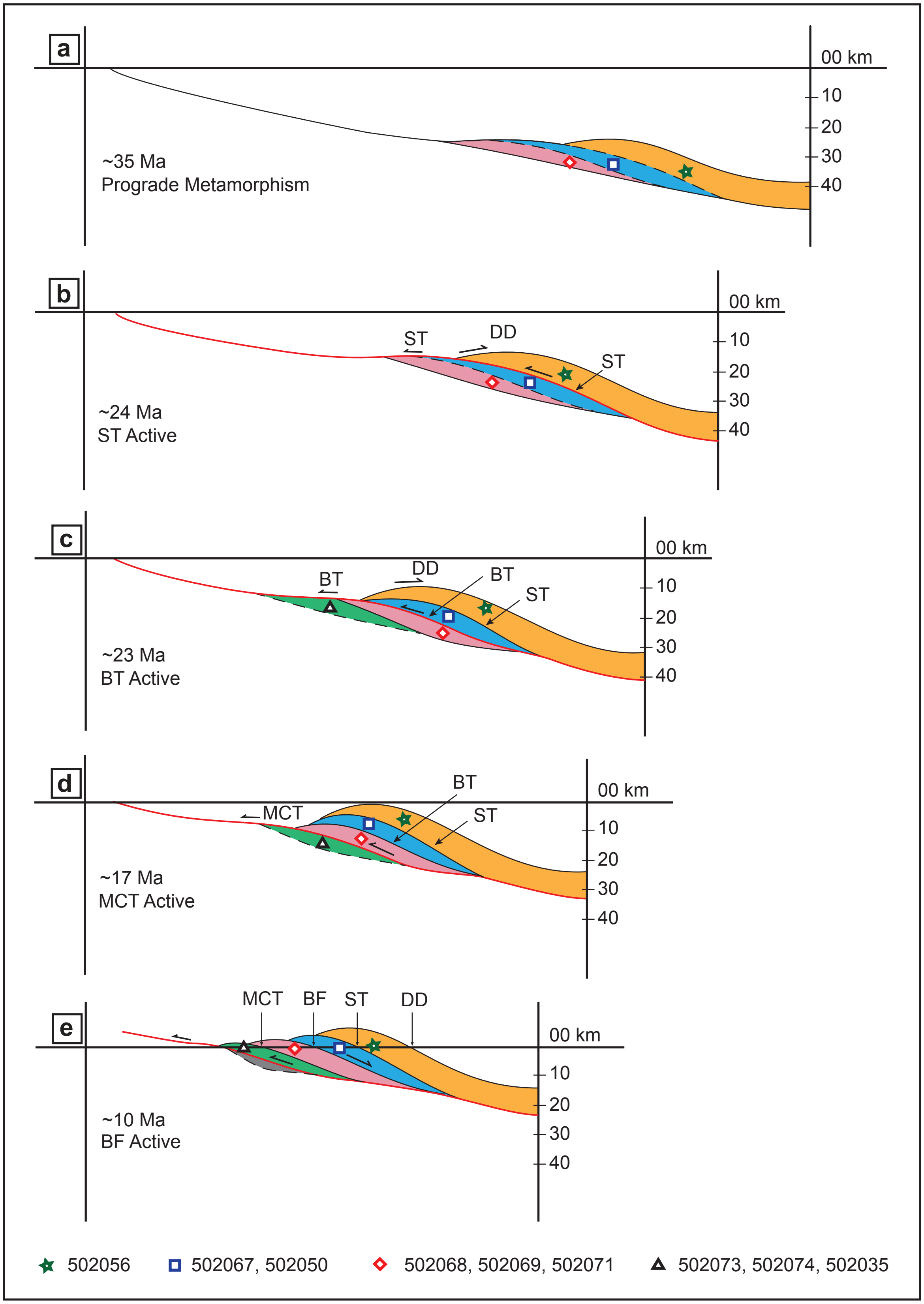

Fig. 15. Schematic kinematic model of the evolution of the rock packages in the study area based on the results presented herein and previously published constraints (Larson et al., 2015, 2016).

Tables.

Table 1

Petrographic description of specimens from Modi Khola valley

Specimen	Location*	Lithology and Mineral Assemblage[#]	Textural Observation (Refer to Fig. 2 and 3)	Garnet Characteristics (Refer to Fig. 2 and 3)
502074	**LHS**	Micaceous phyllitic schist *Major phases* - Qz + Pl + Ms + Bt + Grt + Chl *Accessory phases* - Tur + Ep + Ilm + Ap	- Preferentially oriented muscovite, biotite and chlorite form the main foliation and partially anastomose large garnet porphyroblasts (Fig. 2a & 3a). - Late biotite and chlorite appears as small flakes statically overgrowing the foliation. - Garnet rims are locally replaced by late biotite. - Late chlorite locally overgrow in the matrix and replaces late biotite. - Plagioclase are semi-elongate to equant and form discontinuous lenses parallel to the main foliation. - Quartz are fine grained and elongated parallel to main foliation (Fig. 2a).	- Large porphyroblasts up to 9 mm in diameter (Fig. 2a) - Euhedral to subhedral - Sigmoidal inclusion trails primarily defined by Qz + Ep + Ap inclusions connected to matrix foliation (Fig. 3a) - Monomeneralic inclusions of Qz, Ap, and Ms.
502071	**GHS Unit 1**	Two - mica schist *Major phases* - Qz + Pl + Ms + Bt ± Grt + Chl *Accessory phases* - Ep + Ilm + Ap + Mnz	- Oriented muscovite, biotite and weakly alligned semi-elongate plagioclase form the main foliation. - Muscovite and biotite laths anastomose garnet porphyroblasts (Fig. 3b). - Biotite and chlorite appears to locally replace garnet at the rims (Fig. 3c). - Late chlorite locally overgrow biotite in the matrix. - Plagioclase are semi-elongate to equant and are mostly associted with quartz in the matrix and in strain shadow of garnet porphyroblast (Fig. 3b). - Quartz occurs as medium, semi-elongate grain in the matrix and equant as inclusions in garnet (Fig. 3b,c).	- Large porphyroblasts up to 5 mm in diameter (Fig. 2b) - Euhedral to subhedral - Monomeneralic inclusions of Qz, Ap, and Ilm (Figs. 3b,c)
502068	**GHS Unit 1**	Two - mica schist *Major phases* - Qz + Pl + Ms + Bt + Grt *Accessory phases* - Chl + Tur + Ep + Ilm + Ap + Mnz	- Main foliation is defined by the preferentially oriented biotite and muscovite (Fig. 3d). - Garnet porphyroblast are scattered (Fig. 3d) and typically show inclusion rich cores and inclusion free rims (Fig. 3e). - At most places biotite appears to share straight contact with garnet, but locally late biotite replaces garnet at the rims. - Late chlorite locally overgrow biotite in the matrix and near garnet. - Large plagioclase grains are semi- elongate to equant and dispersed throughout matrix (Fig. 3d). - Quartz are granoblastic and semi elongate along main foliation (Fig. 3d).	- Porphyroblasts up to 1.3 mm in diameter (Fig. 2c) - Euhedral to subhedral - Garnet core with inclusions primarily of of lobate Qz and minor Ep, Ap and Ilm (Fig. 3e) - Outer core is marked by presence of "nanogranites" with polymineralic inclusions of Qz, Bt, Ap, Alm, Rt reflecting peritectic garnet growth (Fig. 3e)

* Refer to Fig. 1 for location of selected specimens.

[#] Abbreviations for minerals after Whitney and Evans (2010).

Specimen	Location*	Lithology and Mineral Assemblage#	Textural Observation (Refer to Fig. 2 and 3)	Garnet Characteristics (Refer to Fig. 2 and 3)
502067	**GHS Unit 1**	Kyanite mica schist *Major phases* - Qz + Pl + Ms + Bt + Grt + Ky + Chl *Accessory phases* - Tur + Zrn + Ap + Mnz + Ilm + Rt	- Biotite and aligned kyanite form the main foliation (Fig. 3f). - Garnet typically show inclusion rich cores and inclusion free rim. - Plagioclase form semi- elongate to equant porphyroblast weakly alingned along the foliation. - Kyanite occurs as elongated blade, and appears to grow on an early biotite and muscovite laths (Fig. 3f). - Muscovite mostly occur as laths growing together with biotite in the matrix or replacing kyanite and garnet (Fig. 3g). - Late chlorite overgrows biotite and garnet.	- Porphyroblasts up to 1.3 mm in diameter (Fig. 2d) - Commonly associated and in close contact with biotite and rarely with plagioclase (Fig. 3g). - Euhedral to subhedral - Core with large inclusion of lobate Qz surrounded by inclusions of Qz, Bt, Ms, Ky, Rt, Ilm, Ap (Fig. 3g)
502050	**GHS Unit 1**	Kyanite mica schist *Major phases* - Qz + Pl + Ms + Bt + Grt + Ky + Chl *Accessory phases* - Zrn + Ap + Mnz + Ilm + Rt	- Strongly oriented biotite and muscovite form the main schistosity (Fig. 3h,i). - Garnet grains are abundant and typically show inclusion rich cores with inclusion free rim (Fig. 3j). - Quartz are granoblastic and semi-elongated along main foliation. - Plagioclase form large porphyroblasts and are typically associated with quarz layers. - Biotite and late chlorite appears to replace garnet at rims. - Kyanite appears as weakly aligned porphyroblast with an emabyed apperance, and is typically replaced by quartz and biotite (Fig. 3i).	- Porphyroblasts up to 2 mm in diameter (Fig. 2e) - Commonly associated and in close contact with biotite and quartz (Fig. 3h). - Euhedral to subhedral - Core with inclusion of Qz and Bt surrounded by polymineralic inclusions of Qz, Bt, Ms, Rt, Ilm, Ap (Fig. 3j).
502056	**GHS Unit 3**	Orthogneiss *Major phases* - Qz + Kfs + Pl + Ms + Bt + Grt *Accessory phases* - Chl + Zrn + Ap + Mnz + Ilm + Rt	- Very weak foliation defined by biotite and rare muscovite. - Large garnet porphyroblasts show inclusion rich cores with thick inclusion free rim overgrowth and associated strain shadows (Fig. 3k). - Biotite and muscovite over grow garnet at the rims and along the strain shadow, and replaces plagioclases in the matrix (Fig. 3k,l). - K-feldspar and plagioclase form large porphyroblasts and show mermekyte textures (Fig. 3l).	- Large porphyroblasts up to 6 mm in diameter (Fig. 2f) - Mostly euhedral - Garnet core with inclusions of lobate Qz and, Pl , Bt, Ap, Rt (Fig. 3k).

* Refer to Fig. 1 for location of selected specimens.
# Abbreviations for minerals after Whitney and Evans (2010).

Table 2

Observed mineral assemblages

Specimen	Rock Type	Mineral assemblage (Modal proportion %)[#]								Accessory phases (< 1%)
		Qz	Pl	Kfs	Bt	Ms	Grt	Ky	Chl	
502074	Garnet Phyllitic Schist	36.5	4.0	-	2.5	43.0	3.0	-	10.5	Tur + Ep + Ilm + Ap
502071	Garnet Mica Schist	42.0	6.5	-	14.5	31.0	5.0	-	1.0	Ep + Ilm + Ap + Mnz
502068	Garnet Mica Schist	34.5	24.5	-	20.5	15.0	5.0	-	-	Chl + Tur + Ep + Ilm + Ap + Mnz
502067	Garnet - Kyanite Mica Schist	56.5	15.0	-	19.0	1.5	2.5	5.0	-	Chl + Tur + Zrn + Ap + Mnz + Ilm + Rt
502050	Garnet - Kyanite Mica Schist	23.5	22.5	-	28.5	18.0	4.5	2.5	-	Chl + Zrn + Ap + Mnz + Ilm + Rt
502056	Garnet Meta-granite	35.5	33.0	16.5	10.5	1.5	2.5	-	-	Chl + Zrn + Ap + Mnz + Ilm + Rt

[#] Abbreviations for minerals after Whitney and Evans (2010).

Table 3

XRF Bulk composition (wt%) used for phase equilibria modelling

Specimen	MnO	Na_2O	CaO	K_2O	Fe_2O_3	MgO	Al_2O_3	SiO_2	P_2O_5	TiO_2	LOI	Total
502074	0.05	1.19	0.64	3.99	5.52	2.44	20.83	60.83	0.12	0.66	4.26	100.53
502071	0.05	0.93	0.41	4.54	6.68	2.02	15.59	65.99	0.16	0.77	3.06	100.20
502068	0.12	2.26	1.56	3.73	7.38	3.18	16.01	63.33	0.19	0.8	2.2	100.76
502067	0.05	1.43	0.54	2.13	4.85	3.16	11.66	74.24	0.15	0.66	1.72	100.59
502050	0.15	2.17	1.11	4.68	9.13	4.05	20.27	55.12	0.23	0.93	2.65	100.49
502056	0.18	2.36	1.51	4.35	4.39	1.28	12.78	72.08	0.21	0.54	1.00	100.68

Table 4

Bulk compositiions in cation moles used as input for phase equilibria modelling in the system MnNCKFMASHTO

Specimen	Mn	Na	Ca	K	Fe (Fe^{2+})	Mg	Al	Si	H	Ti	O (Fe^{3+})*	Total
502074 [a]	0.042	2.269	0.550	5.006	4.050	3.578	24.146	59.830	0.000	0.488	0.041	100.00
502071 [a]	0.042	1.784	0.424	5.731	4.931	2.980	18.182	65.303	0.000	0.573	0.050	100.00
502068 [a]	0.098	4.224	1.353	4.587	5.306	4.569	18.187	61.043	0.000	0.580	0.054	100.00
502068 [b]	0.089	3.838	1.229	4.168	4.821	4.152	16.527	55.470	9.129	0.527	0.049	100.00
502067 [a]	0.041	2.697	0.408	2.643	3.519	4.583	13.368	72.221	0.000	0.483	0.036	100.00
502067 [b]	0.039	2.532	0.383	2.482	3.304	4.302	12.550	67.802	6.119	0.453	0.033	100.00
502050 [a]	0.122	4.050	0.911	5.748	6.556	5.812	22.998	53.063	0.000	0.674	0.066	100.00
502050 [b]	0.108	3.578	0.804	5.077	5.791	5.135	20.316	46.876	11.661	0.595	0.058	100.00
502056 [a]	0.146	4.381	1.336	5.314	3.135	1.827	14.422	69.018	0.000	0.389	0.032	100.00
502056 [b]	0.133	4.003	1.221	4.855	2.864	1.669	13.176	63.055	8.639	0.355	0.029	100.00

[a] Bulk recalculated to model excess H_2O; [b] Bulk recalculated to model saturated solidus.

* Fe^{3+} was taken to be 1% of total Fe (Fe^{2+} + Fe^{3+}).

Table 5

Raman data and calculated QuiG pressures

Specimen No.	Analyzed		Max Raman Shift	Residual Pressure	Temperature	Max Pressure
	Garnets	Inclusions	$\Delta\nu_{464}$ (cm^{-1})	P_{incl} (kbar)	T (℃)	P (kbar)
502056	6	13	1.43 ± 0.10	1.58 ± 0.22	695	11.0 ± 0.2
Sinuwa Thrust						
502050	6	20	1.70 ± 0.18	1.87 ± 0.22	680	11.2 ± 0.3
502067	11	17	1.73 ± 0.19	1.91 ± 0.22	675	11.1 ± 0.3
Bhanuwa Fault						
502068	6	18	2.19 ± 0.14	2.41 ± 0.22	675	11.9 ± 0.3
502069	6	15	2.85 ± 0.11	3.15 ± 0.23	675	13.1 ± 0.2
502071	8	13	2.24 ± 0.17	2.47 ± 0.22	600	10.9 ± 0.3
MCT						

Table 6

Garnet Lu-Hf isotope and age data

Sample Fraction	Lu (ppm)	Hf (ppm)	$^{176}Lu/^{177}Hf$	2 s.d.	$^{176}Hf/^{177}Hf$	2 s.d.	Isochron age (Ma)	MSWD	Initial 176Hf/177Hf
502074									
Grt-1	2.13	0.099	3.054	0.008	0.282424	0.000032			
Grt-2	2.14	0.113	2.675	0.007	0.282276	0.000036			
Grt-3	2.40	0.075	4.531	0.011	0.282860	0.000037			
Grt-4	2.21	0.111	2.826	0.007	0.282309	0.000031			
WR-1	0.34	4.21	0.01145	0.00009	0.281448	0.000024			
							16.8 ± 0.5	1.3	0.281444 ± 0.000023
502071									
Grt-1	25.6	0.0686	52.88	0.13	0.315631	0.000054			
Grt-2	25.1	0.0515	69.06	0.17	0.325837	0.000064			
Grt-3	23.2	0.0668	49.27	0.12	0.313424	0.000056			
Grt-4	24.4	0.0497	69.59	0.17	0.326237	0.000078			
WR-1	0.765	6.38	0.017	0.00004	0.282039	0.000026			
							34.0 ± 0.1	1.6	0.282030 ± 0.000025
502068									
Grt-1	13.8	0.122	16.080	0.040	0.292514	0.000046			
Grt-2	14.9	0.230	9.156	0.023	0.287937	0.000043			
Grt-3	15.2	0.266	8.124	0.020	0.287319	0.000048			
Grt-4	13.2	0.194	9.667	0.024	0.288312	0.000041			
WR-1	0.52	4.8	0.01536	0.00004	0.281991	0.000027			
							35.1 ± 0.2	1.1	0.281980 ± 0.000025
502067									
Grt-1	7.07	0.160	6.261	0.016	0.285015	0.000045			
Grt-2	6.6	0.108	8.686	0.022	0.286291	0.000034			
Grt-3	7.45	0.218	4.843	0.012	0.284254	0.000031			
Grt-4	6.92	0.283	3.469	0.009	0.283512	0.000030			
WR-1	0.425	6.21	0.009696	0.00002424	0.281773	0.000023			
							27.8 ± 0.2	1.7	0.281762 ± 0.000022
502056									
Grt-1	94.5	0.0311	430.9	1.1	0.561944	0.000074			
Grt-2	87.7	0.0306	405.8	1.0	0.544792	0.000096			
Grt-3	88.4	0.0339	369.8	0.9	0.521594	0.000081			
WR-1	2.64	5.85	0.0639	0.00016	0.282025	0.000026			
							34.7 ± 0.1	1.9	0.281983 ± 0.000025

Note: Age uncertainities represent absolute 2 s.d. MSWD = mean square of weighted deviates